

# Ab initio studies of influence of periodic-direction electric fields on spin lifetime and spin diffusion length and the validation of an *ab initio* matrix-drift-diffusion model

Junqing Xu,<sup>1,\*</sup> Can Liu,<sup>1</sup> and Weiwei Chen<sup>1,†</sup>

<sup>1</sup>Department of Physics, Hefei University of Technology, Hefei, Anhui 230601, China

(Dated: January 22, 2026)

Recently, we developed an *ab initio* approach of spin lifetime ( $\tau_s$ ) and spin diffusion length ( $l_s$ ) in solids [Phys. Rev. Lett. 135, 046705 (2025)], based on a density-matrix master equation with quantum treatment of electron scattering processes. In this work, we extend the method to include the drift term due to an electric field along a periodic direction, implemented using a Wannier-representation-based covariant derivative. We employ this approach to investigate the electric-field effect on  $\tau_s$  and  $l_s$  of monolayer WSe<sub>2</sub>, bulk GaAs, bulk GaN, and graphene-*h*-BN heterostructure. We find that an electric field reduces  $\tau_s$  of GaAs, due to the induced D'yakonov-Perel' type spin relaxation. In GaN and graphene-*h*-BN,  $\tau_s$  is significantly affected, partly because the electric field generates an effective magnetic field corresponding to the  $k$ -derivative of Rashba spin-orbit (magnetic) field. Our results show that  $l_s$  can be significantly enhanced or suppressed by a moderate downstream or upstream field respectively. While the standard drift-diffusion model performs well for WSe<sub>2</sub>, it can introduce large errors of the electric-field-induced changes of  $l_s$  in GaAs, GaN and graphene-*h*-BN. Our proposed *ab initio* matrix-drift-diffusion model improves results for GaAs and GaN, but still fails for graphene-*h*-BN. Thus, to accurately capture the influence of electric fields on  $l_s$  in realistic materials, it is necessary to go beyond the drift-diffusion model and adopt a microscopic *ab initio* methodology. Moreover, in graphene-*h*-BN, we find that the field-induced changes of  $\tau_s$  and  $l_s$  are not only governed by the drift term in the master equation, but are also significantly affected by the electric-field modification of the equilibrium density matrix away from Fermi-Dirac distribution function.

## I. INTRODUCTION

Spin lifetime ( $\tau_s$ ) and spin diffusion length ( $l_s$ ) are key parameters for spintronic device applications, which aim to achieve the next generation of low-power electronics by making use of the spin degree of freedom[1–3]. In spintronic devices, sufficiently long  $\tau_s$  and  $l_s$  are typically required within the spin transport channel to ensure stable spin detection and manipulation. Accurate simulations of  $\tau_s$  and  $l_s$  are invaluable to predict promising spintronic materials with long enough  $\tau_s$  and  $l_s$  and optimizing device operating conditions. Recently, we developed an *ab initio* approach of both  $\tau_s$  and  $l_s$  in solids, based on a density-matrix master equation with quantum treatment of electron scattering processes[4]. It has been successfully applied to disparate materials—including 2D and 3D semiconductors, graphene-*h*-BN heterostructure, the heavy metal Pt and the antiferromagnet RuO<sub>2</sub>—yielding theoretical results in good agreement with experimental measurements[3, 5–9].

While our approach can readily incorporate an electric field (**E**) along a non-periodic direction at the density-functional-theory (DFT) level[10, 11], the treatment of a field along a periodic direction remained challenging. This capability is crucial for applications, as a longitudinal **E**—essential for driving charge carriers and their associated spins in devices—can significantly modulate  $l_s$  via spin-drift effect[2, 12–17]. Consequently, accurate simu-

lation of this effect is critical for the predictive modeling of spintronic devices.

Spin-drift effect has been investigated both theoretically and experimentally by several groups. In semiconductors, its influence on  $l_s$  is often estimated using the following drift-diffusion model:  $D\nabla^2 S(\mathbf{r}) \pm \mu \mathbf{E} \cdot \nabla S(\mathbf{r}) = S(\mathbf{r}) / \tau_s$ , with  $\pm$  corresponding to electrons or holes.  $\mu$  is carrier mobility.  $D$  is diffusion coefficient. By solving this equation and defining  $\eta = \mu/D$ , the following model formula of  $l_s(E)$  is obtained[2, 12, 17]

$$\frac{1}{l_s(E)} = \sqrt{\frac{1}{l_{s0}^2} + \frac{E^2}{4} \frac{\mu^2}{D^2} - \theta \frac{|E|}{2} \frac{\mu}{D}}, \quad (1)$$

where  $l_{s0}$  is the zero-electric-field spin diffusion length.  $\theta$  is  $\pm$  for downstream or upstream fields respectively. However, as pointed out in our recent *ab initio* work, the drift-diffusion model may cause significant errors of  $l_s$  in specific systems such as graphene-*h*-BN and wurtzite GaN, where spatial spin precession substantially influences spin diffusion. It is therefore essential to assess the validity of this model in such systems through direct comparison with *ab initio* results. Other theoretical studies have employed more sophisticated transport equations[2] to simulate spin-drift effect on  $l_s$ . Nonetheless, these works typically rely on model Hamiltonians and simplified treatments of scattering processes, and thus are lack of predictive accuracy and broad applicability.

The effect of a periodic-direction electric field on  $\tau_s$  was also studied experimentally and theoretically[2, 18], and was found important to materials, in which spin relaxation is dominated by D'yakonov-Perel' mechanism.

\* jqxu@hfut.edu.cn

† chenweiwei@hfut.edu.cn

Previous theoretical studies have relied on model Hamiltonians, so that fully *ab initio* simulations are valuable to improve the understandings of the electric-field effects.

Here we extend our recently developed *ab initio* approach of  $\tau_s$  and  $l_s$  to include the drift term due to a uniform dc electric field along a periodic direction, using a covariant derivative formalism. The extension enables accurate simulation of the electric-field effect on  $\tau_s$  and  $l_s$  across a wide range of materials, thereby fully addressing the above issues.

The paper is organized as follows. In Sec. II A, we derive the linearized quantum master equation for electron dynamics and transport under finite  $\mathbf{E}$ . We then describe how to simulate  $\tau_s(E)$  and  $l_s(E)$  via solving full eigenvalue problems (EVPs). Section II B introduces several approximate methods: first, calculations based on Rayleigh-Ritz (RR) method; second, an *ab initio* matrix-drift-diffusion (ab-mDD) model; and third, three model formulas of  $l_s(E)$  from the standard drift-diffusion model. In Sec. III, we present theoretical results of  $\tau_s(E)$  and  $l_s(E)$  by our *ab initio* approach, compared with estimates from approximate methods, for monolayer WSe<sub>2</sub>, bulk GaAs, bulk GaN and graphene-*h*-BN. At the end, a summary and outlooks are given.

## II. METHODS

### A. The linearized quantum master equation under finite $\mathbf{E}$ and the computations of $\tau_s$ and $l_s$

#### 1. The linearized master equation

We obtain the linearized master equation following the strategy of our prior paper[4] with a few electric-field-related modifications. To simulate the electron transport, we apply the Wigner transformation to the quantum (density-matrix) master equation and obtain[4, 19]

$$\frac{d\rho_{\kappa}^{\text{tot}}(t, \mathbf{R})}{dt} + \frac{1}{2} \left\{ \mathbf{v} \cdot \frac{d\rho^{\text{tot}}(t, \mathbf{R})}{d\mathbf{R}} \right\}_{\kappa} = -\frac{i}{\hbar} [H^e(\mathbf{B}), \rho^{\text{tot}}]_{\kappa} + D^E[\rho^{\text{tot}}] + C_{\kappa}[\rho^{\text{tot}}], \quad (2)$$

Where  $\kappa = \{k, a, b\}$  is the combined index of k-point and two band indices.  $\mathbf{R}$  is real-space coordinate.  $\rho^{\text{tot}}(t, \mathbf{R})$  is the total electronic Wigner distribution function corresponding to the total density matrix.  $\frac{1}{2} \{ \mathbf{v} \cdot \nabla_{\mathbf{R}} \rho^{\text{tot}} \}_{\kappa}$  is the diffusion term with  $\mathbf{v}$  the vector of velocity matrices.  $\{\mathbf{a} \cdot \mathbf{b}\} = \mathbf{a}\mathbf{b} + \mathbf{b}\mathbf{a}$ . The right-hand-side terms are the coherent, drift and scattering terms respectively.  $H^e(\mathbf{B}) = H^e(0) + H^{\text{SZ}}(\mathbf{B})$ , with  $H^{\text{SZ}}(\mathbf{B}) = \mu_B g_0 \mathbf{B} \cdot \mathbf{s}$  being spin Zeeman Hamiltonian. The drift term  $D^E[\rho^{\text{tot}}]$  under finite  $\mathbf{E}$  along a periodic direction reads[19–21]

$$D^E[\rho^{\text{tot}}] = \frac{e}{\hbar} \mathbf{E} \cdot \frac{D\rho^{\text{tot}}}{D\mathbf{k}}, \quad (3)$$

$$\frac{DA_k}{D\mathbf{k}} = \frac{dA_k}{d\mathbf{k}} - i[\xi_k, A_k], \quad (4)$$

with  $\frac{DA_k}{D\mathbf{k}}$  the covariant derivative of matrix  $A_k$  and  $\xi$  the Berry connection in the eigenstate representation.

Within Born-Markov approximation and neglecting the renormalization part[22–24], the scattering term  $C[\rho^{\text{tot}}]$  is quadratic functional of  $\rho^{\text{tot}}$  and the detailed form is given in Ref. 23. The above assumptions for  $C[\rho^{\text{tot}}]$  are commonly employed and typically valid in studies of  $\tau_s$  or  $l_s$ , which focus on slow decay processes in systems that are usually not far from equilibrium. Their justifications were discussed in Ref. 23.

Suppose  $\rho^{\text{tot}} = \rho^{\text{eq}} + \rho$ , with  $\rho^{\text{eq}}$  the equilibrium density matrix. At  $\mathbf{E}=0$ ,  $\rho^{\text{eq}}$  becomes Fermi-Dirac function  $f$ . Assuming  $\rho$  is small, typical in device applications and measurements of  $\tau$  and  $l$ , we obtain a linearized master equation by linearizing the scattering term[4]

$$\frac{d\rho_{\kappa}}{dt} + \sum_{j\kappa'} L_{\kappa\kappa'}^{v_j} \frac{d\rho_{\kappa'}}{dR_j} = \sum_{\kappa'} L_{\kappa\kappa'}(\mathbf{E}, \mathbf{B}) \rho_{\kappa'}, \quad (5)$$

$$L(\mathbf{E}, \mathbf{B}) = L^v(\mathbf{B}) + L^E(\mathbf{E}) + L^C, \quad (6)$$

where  $L^{v_j}$ ,  $L^v$ ,  $L^E$  and  $L^C$  correspond to the diffusion, coherent, drift and scattering terms respectively.  $L^{v_j}$  and  $L^v$  are given in Appendix A. For the electron-phonon (e-ph) scattering,  $L^C$  reads

$$L_{kab, k'cd}^C = \bar{L}_{kab, k'cd}^C + \bar{L}_{kba, k'dc}^{C,*}, \quad (7)$$

$$\begin{aligned} \bar{L}_{kab, k'cd}^C = & \frac{1}{2N_k} \sum_e [(I - \rho^{\text{eq}})_{kae} P_{keb, k'cd} + P_{k'cd, kae}^* \rho_{keb}^{\text{eq}}] \\ & - \frac{1}{2N_k} \delta_{kk'} \delta_{ac} \sum_{k''fg} P_{kdb, k''fg} \rho_{k''fg}^{\text{eq}} \\ & - \frac{1}{2N_k} \delta_{kk'} \sum_{k''fg} (I - \rho^{\text{eq}})_{k''fg} P_{k''fg, kac}^* \delta_{bd}. \end{aligned} \quad (8)$$

where  $P$  is the generalized scattering-rate matrix.  $P$  is computed from first-principles electron and phonon energies and the e-ph matrix elements.[23] Eqs. 7–8 are slightly different from those in our prior paper[4], where  $\rho^{\text{eq}}$  is fixed as Fermi-Dirac function  $f$ . We emphasized that to obtain the linearized master equation (Eq. 5) from the nonlinear equation (Eq. 2), only the scattering term  $C[\rho^{\text{tot}}]$  is linearized. The other terms in Eq. 2 remain unchanged but are reformulated. Consequently, our treatment of the electric field is applicable over a range potentially several orders of magnitude wider than that studied here.

The quantum master equation presented above is closely connected to standard Boltzmann transport equation and kinetic spin Bloch equation. We compare them in Appendix B.

#### 2. The finite-difference computation of $L^E$ based on Wannier functions

Given that  $L^E \rho = D^E[\rho]$  and the form of  $D^E$  in Eq. 3, to express matrix  $L^E$ , we first need to express the co-

variant derivative  $\frac{D\rho}{D\mathbf{k}}$  via finite differences. However, a direct computation of  $\frac{D\rho}{D\mathbf{k}}$  via Eq. 4 is non-trivial due to the following issues: First, the basis functions  $u$  are usually obtained by diagonalizing  $H^0$  at different  $\mathbf{k}$  independently, so that  $u$  contain arbitrary phase factors and are arbitrary in degenerate subspaces. Therefore,  $u$  are in general not smooth over  $\mathbf{k}$ , which makes  $\frac{d\rho}{d\mathbf{k}}$  not well-defined. Second, the computation of  $\xi$  usually relies on the non-degenerate perturbation theory, which may be problematic in the presence of band degeneracies or crossings. These issues are bypassed by using a Wannier-representation finite-difference technique, which has been employed to compute  $\frac{D\rho}{D\mathbf{k}}$  for nonlinear photocurrent simulation[20, 25].

To make this work self-contained, we present the expression of  $\frac{D\rho}{D\mathbf{k}}$  follows the algorithm of our prior paper[20] below, but with a differences: Previous work[20] relies on relaxation-time approximation, so that all  $k$ -points are decoupled and  $\frac{D\rho}{D\mathbf{k}}$  can be evaluated using finite differences between arbitrarily-close neighboring  $k$ -points. Whereas here, we need to carry out finite differences between selected  $k$ -points from uniform  $k$  meshes and cares must be taken for boundary  $k$ -points of selected ones (see  $k$ -point selection in Appendix I). Additionally, we do not directly compute  $\frac{D\rho}{D\mathbf{k}}$  here, and instead we compute  $L^E$  matrix, whose formula is derived from that of  $\frac{D\rho}{D\mathbf{k}}$ .

The Wannier functions are noted as  $|\mathbb{R}a\rangle$ , where  $a$  is the index of a Wannier function in the unitcell and  $\mathbb{R}$  labels the unitcell. The smooth Bloch-like functions are given by the phased sum of Wannier functions[26]

$$|u_{ka}^W\rangle = \sum_{\mathbb{R}} e^{-i\mathbf{k}\cdot(\hat{\mathbf{r}}-\mathbb{R})} |\mathbb{R}a\rangle, \quad (9)$$

which span the actual Bloch eigenstates  $|u_{ka}\rangle$  at each  $\mathbf{k}$ .  $\hat{\mathbf{r}}$  is position operator. Here a hat is used to emphasize that it is an operator instead of a coordinate of electron position.

Define

$$\widehat{H}_k^e = e^{-i\mathbf{k}\cdot\hat{\mathbf{r}}} \widehat{H}^e e^{i\mathbf{k}\cdot\hat{\mathbf{r}}}, \quad (10)$$

with  $\widehat{H}^e$  the electronic Hamiltonian operator.

It follows that, if we construct the Hamiltonian in the Wannier representation

$$H_{kab}^W = \langle u_{ka}^W | \widehat{H}_k^0 | u_{kb}^W \rangle, \quad (11)$$

and diagonalize it as

$$U_k^\dagger H_k^W U_k = \epsilon_k, \quad (12)$$

we obtain the diagonal matrix of eigenvalues  $\epsilon_k$  and the eigenstate matrix  $U_k$ .

Define  $\rho_k^W = U_k \rho_k U_k^\dagger$  as the Wigner function in Wannier representation. According to Refs. 20 and 25, the

covariant derivative  $\frac{D\rho}{D\mathbf{k}}$  satisfies:

$$\frac{D\rho_k}{D\mathbf{k}} = U_k^\dagger \frac{D\rho_k^W}{D\mathbf{k}} U_k, \quad (13)$$

$$\frac{D\rho_k^W}{D\mathbf{k}} = \frac{d\rho_k^W}{d\mathbf{k}} - i [\xi_k^W, \rho_k^W], \quad (14)$$

where  $\xi^W$  is Berry connection in Wannier representation. In Wannier representation, the basis  $u_{ka}^W$  are smooth over  $\mathbf{k}$ , so that  $\frac{D\rho_k^W}{D\mathbf{k}}$  can be accurately computed via finite differences:

$$\frac{D\rho_k^W}{Dk_\alpha} = \frac{\rho_{k_\alpha^+}^W - \rho_{k_\alpha^-}^W}{2dk_\alpha} - i [\xi_{k_\alpha}^W, \rho_k^W], \quad (15)$$

where  $k_\alpha^\pm = k_\alpha \pm dk_\alpha$ .

From Eqs. 3, 13 and 15, we have

$$D^E [\rho] = \sum_{\alpha} \frac{eE_{\alpha}}{\hbar} \frac{o^{kk_{\alpha}^+} \rho_{k_{\alpha}^+} o^{kk_{\alpha}^+, \dagger} - o^{kk_{\alpha}^-} \rho_{k_{\alpha}^-} o^{kk_{\alpha}^-, \dagger}}{2d\mathbf{k}} - i \sum_{\alpha} \frac{eE_{\alpha}}{\hbar} [\xi_{k_{\alpha}}^W, \rho_k], \quad (16)$$

$$o^{k_1 k_2} = U_{k_1}^\dagger U_{k_2}, \quad (17)$$

$$\bar{\xi}_k = U_k^\dagger \xi_k^W U_k. \quad (18)$$

Therefore,

$$L^E = \sum_{\alpha} E_{\alpha} L_{\alpha}^E, \quad (19)$$

$$L_{\alpha, kabk'cd}^E = \frac{e}{\hbar} \frac{o_{ac}^{kk_{\alpha}^+} (o^{kk_{\alpha}^+, \dagger})_{db} \delta_{k'k_{\alpha}^+}}{2d\mathbf{k}} - \frac{e}{\hbar} \frac{o_{ac}^{kk_{\alpha}^-} (o^{kk_{\alpha}^-, \dagger})_{db} \delta_{k'k_{\alpha}^-}}{2d\mathbf{k}} - \frac{ie}{\hbar} (\bar{\xi}_{kac} \delta_{bd} - \delta_{ac} \bar{\xi}_{kdb}) \delta_{kk'}. \quad (20)$$

For boundary  $k$ -points, the derivatives are expressed via simple finite differences instead of central ones, so that the formula of  $L^E$  is slightly different from the above formula but its derivation is straightforward.

### 3. The solution of $\rho^{\text{eq}}$ under finite $\mathbf{E}$

Since  $\rho^{\text{eq}}$  is here independent of both  $t$  and  $\mathbf{R}$ , from Eq. 2,  $\rho^{\text{eq}}$  satisfies

$$-\frac{i}{\hbar} [H^e, \rho^{\text{eq}}] + D^E [\rho^{\text{eq}}] + C [\rho^{\text{eq}}] = 0. \quad (21)$$

Suppose  $\rho^{\text{eq}} = f + \delta\rho^{\text{eq}}$ .  $C [\rho^{\text{eq}}]$  can be separated into a linear part  $L^C [f]$  and a quadratic part  $M [\delta\rho^{\text{eq}}]$ ,

$$C [\rho^{\text{eq}}] = L^C [f] \delta\rho^{\text{eq}} + M [\delta\rho^{\text{eq}}]. \quad (22)$$

$$M_{kab}[\delta\rho^{\text{eq}}] = \frac{1}{2} \sum_{ck'de} \begin{pmatrix} -\rho_{kac} P_{kcb,k'de} \rho_{k'de} \\ +\rho_{k'de} P_{k'de,kac}^* \rho_{kcb} \end{pmatrix} + H.C.. \quad (23)$$

Note that Eq. 22 is exact and is applicable to large  $\delta\rho^{\text{eq}}$ . In Eq. 22, the coefficient matrix of the linear part  $-L^C[f]$  is a fixed matrix, which facilitates the iterative solution for  $\rho^{\text{eq}}$  described in the following.

To derive the above equations, we have considered  $C[f]=0$ , reflecting the fact that there is no scattering at equilibrium without electric field.

Considering that  $D^E[\rho^{\text{eq}}]=L^E f + L^E \delta\rho^{\text{eq}}$  and defining  $\tilde{L}\delta\rho^{\text{eq}}=(L^e + L^E + L^C[f])\delta\rho^{\text{eq}}$ , from Eq. 21, we have

$$L^E f + \tilde{L}\delta\rho^{\text{eq}} + M[\delta\rho^{\text{eq}}] = 0. \quad (24)$$

This can be rewritten as

$$\delta\rho^{\text{eq}} = -(\tilde{L})^{-1} \{ L^E f + M[\delta\rho^{\text{eq}}] \}. \quad (25)$$

Therefore,  $\delta\rho^{\text{eq}}$  can be solved by fixed-point iteration with a mixing parameter  $\alpha^{\text{mix}}$ :

$$\delta\rho^{\text{eq},(n+1)} = (1 - \alpha^{\text{mix}}) \delta\rho^{\text{eq},(n)} + \alpha^{\text{mix}} \delta\rho_0^{\text{eq},(n+1)}, \quad (26)$$

$$\delta\rho_0^{\text{eq},(n+1)} = -(\tilde{L})^{-1} \{ L^E f + M[\delta\rho^{\text{eq},(n)}] \}, \quad (27)$$

$$\delta\rho_0^{\text{eq},(1)} = -(\tilde{L})^{-1} L^E f, \quad (28)$$

with  $\delta\rho^{\text{eq},(n)}$  being  $\delta\rho^{\text{eq}}$  at  $n$ th iteration. In all calculations with  $\mathbf{E}\neq 0$ , we numerically iterate until the absolute and relative errors of  $\delta\rho^{\text{eq}}$  fall below  $10^{-12}$  and  $10^{-6}$  respectively. The fully converged  $\delta\rho^{\text{eq}}$  is then used to compute the scattering term  $L^C[\rho^{\text{eq}}]$  (the other terms in Eq. 5 do not depend on  $\rho^{\text{eq}}$ ). According to our numerical tests, we find that  $-(\tilde{L})^{-1} L^E f$  is already a good approximation of  $\delta\rho^{\text{eq}}$  within our studied electric-field range.

#### 4. The computations of $\tau_s$ and $l_s$ via solving a full EVP

This part was described in our prior paper[4], we present it here to make this work self-contained. To obtain  $\tau_s$  and  $l_s$ , it is required to solve linearized master equation Eq. 5. Here we consider two important commonly used one-variable problems: (i) spatial homogeneous relaxation and (ii) 1D steady-state diffusion along  $x$  direction. The solutions for the relaxation and diffusion problems are[4]

$$\rho_\kappa(t) = \Sigma_\mu e^{-\Gamma_\mu t} U_{\kappa\mu}^{tR} c_\mu^t, \quad (29)$$

$$\rho_\kappa(x) = \Sigma_\nu e^{-\lambda_\nu^x x} U_{\kappa\nu}^{xR} c_\nu^x, \quad (30)$$

respectively.  $\mu$  and  $\nu$  are decay mode indices.  $\Gamma_\mu$  is complex relaxation rate and  $\lambda_\mu^x$  is called complex diffusion rate here.  $\text{Re}\Gamma_\mu$  and  $\text{Re}\lambda_\mu^x$  are decay-mode-resolved lifetime  $\tau_\mu$  and inverse diffusion length  $1/l_\nu^x$ , respectively.

$\text{Im}\Gamma_\mu$  and  $\text{Im}\lambda_\nu^x$  describe temporal and spatial precession, respectively.  $U_{\kappa\mu}^{tR}$  are right eigenvectors of standard EVP with  $\Gamma_\mu$  being the eigenvalues:

$$-\Sigma_{\kappa'} L_{\kappa\kappa'} U_{\kappa'\mu}^{tR} = U_{\kappa\mu}^{tR} \Gamma_\mu. \quad (31)$$

and  $U_{\kappa\nu}^{xR}$  are right eigenvectors of the generalized EVP with  $E_\nu^X=1/\lambda_\nu^x$  being the eigenvalues:

$$\Sigma_{\kappa'} L_{\kappa\kappa'} U_{\kappa'\nu}^{xR} = -\Sigma_{\kappa\kappa'} L_{\kappa\kappa'} U_{\kappa'\nu}^{xR} (\lambda_\nu^x)^{-1}. \quad (32)$$

We consider the boundary conditions:  $\rho(t=0)=\rho^{s_i}$  and  $\rho(t\rightarrow\infty)=0$  for relaxation problem;  $\rho(x=0)=\rho^{s_i}$  and  $\rho(x\rightarrow\infty)=0$  for diffusion problem.  $\rho^{s_i}$  (Eq. 73) is spin perturbative density-matrix induced by spin Zeeman effect[27]. We then obtain  $c_\mu^t = -\sum_\kappa U_{\kappa\mu}^{tL,*} \rho_\kappa^{\text{pert}}$  with  $U_{\kappa\mu}^{tL}$  left eigenvector of Eq. 31, and  $c_\nu^x = -\sum_{\kappa\kappa'} U_{\kappa\nu}^{xL,*} L_{\kappa\kappa'} \rho_{\kappa'}^{\text{pert}}$  with  $U_{\kappa\nu}^{xL}$  left eigenvector of Eq. 32. With the solutions of  $\rho_\kappa(t)$  or  $\rho_\kappa(x)$ , we can then simulate the decay curves of spin observable and obtain  $\tau_s$  and  $l_s$ . See more details in Appendix D.

#### B. Approximate methods of $\tau_s(E)$ and $l_s(E)$

##### 1. Approximate calculation based on Rayleigh-Ritz (RR) method

Low-power electronics often require slow decay of quantities like spin for stable detection and manipulation of information. For slow decay, it seems unnecessary to solve full EVPs (Eq. 32), but enough to obtain eigenvalues and eigenvectors of a few “relevant” modes using approximate methods, e.g., the RR method[28]. In this method, eigenvectors are linear combinations of trial vectors, which span a Krylov subspace (KS)[29] here. For a full EVP  $AU^R = BU^R E$  (Eq. 32), order- $n$  right KS  $V^{KR}$  consists of  $A^{m-l} B^l V^R$  with  $0 \leq l \leq m \leq n$ , where columns of  $V^R$  are trial vectors. Similarly, left KS  $V^{KL}$  consists of  $A^{\dagger, m-l} B^{\dagger, l} V^L$ .

With  $V^{KR(L)}$  and  $M^K = V^{KL,\dagger} M V^{KR}$ , a reduced EVP is obtained

$$A^K Y^R = B^K Y^R E. \quad (33)$$

Eigenvalues of Eq. 33 are approximate eigenvalues of the full EVP (Eq. 32). Eigenvectors  $U^{R(L)} \approx V^{KR(L)} Y^{R(L)}$  if enforcing  $V^{KL,\dagger} B^K V^{KR} = I$ .

Below we specify a few types of trial vectors  $V^{R(L)}$  for approximate spin decay simulations based on low-order RR method.

##### Spin Relaxation:

The corresponding reduced EVP is

$$-(L^{E0K} + L^{EK}) Y^R = I^K Y^R \Gamma_s, \quad (34)$$

where  $L^{E0K} = V^{KL,\dagger} L^{E0} V^{KR}$  with  $L^{E0}$  is  $L$  matrix at  $\mathbf{E}=0$ ,  $L^{EK} = V^{KL,\dagger} L^E V^{KR}$  and  $I^K = V^{KL,\dagger} V^{KR}$ . Here we set

$$V^{R(L)} = \{ U_{sx}^{tR(L)}, U_{sy}^{tR(L)}, U_{sz}^{tR(L)} \}, \quad (35)$$

where  $U_{sa}^{tR(L)}$  is the right (left) eigenvector of Eq. 31 for zero-field relaxation problem, with the eigenvalue being zero-electric-field spin relaxation rate of  $S_\alpha - \Gamma_{s,\alpha}^0$ . We refer to simulations using order- $n$  RR method with such  $V^{R(L)}$  as “ $n$ -RR” simulations here.

### Spin Diffusion:

The corresponding reduced EVP is

$$-(L^{E0K} + L^{EK}) Y^R = L^{v_x K} Y^R \lambda_s, \quad (36)$$

where  $L^{v_x K} = V^{KL,†} L^{v_x} V^{KR}$ . To emphasize the importance of  $V^{R(L)}$  to the RR-based simulation of  $l_s$ , we consider three distinct types of  $V^{R(L)}$ :

(i)  $n$ -RR simulation.

$$V^{R(L)} = \left\{ U_{sx\pm}^{xR(L)}, U_{sy\pm}^{xR(L)}, U_{sz\pm}^{xR(L)} \right\}, \quad (37)$$

where  $U_{sx\pm}^{xR(L)}$  is the right (left) eigenvector of Eq. 31 for zero-field diffusion problem, with the eigenvalue being  $\pm 1/\lambda_{s,\alpha}^0$ .  $\lambda_{s,\alpha}^0$  is zero-electric-field (complex) spin diffusion rate of  $S_\alpha$ .

(ii)  $n$ -RR-B simulation.

$$V^{R(L)} = \left\{ U_s^{tR(L)}, L^{v_x} U_s^{tR(L)} \right\}, \quad (38)$$

$$U_s^{tR(L)} = \left\{ U_{sx}^{xR(L)}, U_{sy}^{xR(L)}, U_{sz}^{xR(L)} \right\}. \quad (39)$$

(iii)  $n$ -RR-C simulation.

$$V^{R(L)} = \left\{ U_s^{cR(L)}, L^{v_x} U_s^{cR(L)} \right\}, \quad (40)$$

$$U_s^{cR} = \{\rho^{s_x}, \rho^{s_y}, \rho^{s_z}\}, \quad (41)$$

$$U_s^{cL} = \{\varrho^{s_x}, \varrho^{s_y}, \varrho^{s_z}\}, \quad (42)$$

where  $\rho^{s_\alpha}$  (Eq. 73) is spin perturbative density matrix introduced above in Sec. II A 4. Its dual vector  $\varrho_s^{s_\alpha}$  satisfies  $\varrho_s^{s_\alpha} \propto s_\alpha$  and  $\langle \varrho_s^{s_\alpha} | \rho^{s_\alpha} \rangle = 1$ . According to our prior paper (Ref. 4),  $\rho^{s_\alpha}$  and  $\varrho_s^{s_\alpha}$  are approximate right and left eigenvectors of the scattering-term matrix  $L^C$ , with the corresponding eigenvalue  $\Gamma_\alpha^{EY}$  approximating the Elliott-Yafet (EY)-type spin relaxation rate arising from spin-flip scattering.

We emphasize that the RR method with KS is a powerful tool for estimating  $\tau_s$  and  $l_s$ . Low-order RR simulations are valuable to provide mechanistic insights, while high-order RR simulations generally improve accuracy. However, the method has limitations: (i) Its accuracy strongly depends on the choices of both  $V^R$  and  $V^L$ . This is particularly critical for low-order simulations. (ii) There is no general guarantee that  $V^{KR}$  and  $V^{KL}$  simultaneously form suitable basis sets for the true right and left eigenvectors, which may lead to significant errors of  $\Gamma_s$ ,  $\lambda_s$  and the corresponding eigenvectors. This issue may be mitigated by employing specific techniques in the KS-based (block) iterative eigensolvers, such as updating the basis according to the residual of the approximate EVP.

## 2. The ab initio matrix-drift-diffusion (ab-mDD) model

Here we derive an advanced theoretical model from linearized master equation. It generalizes the standard drift-diffusion model with several additional physical effects.

Suppose  $V_{\kappa\nu}^{sR}$  and  $V_{\kappa\nu}^{sL}$  ( $\nu=1,2,\dots,N^s$ ) are biorthonormal basis functions of  $\rho$  ( $\langle V_{\kappa\nu}^{sL} | V_{\kappa\nu'}^{sR} \rangle = \delta_{\nu\nu'}$ ) and are highly relevant to spin decay. Define a projector  $P$  and its complement  $Q$  as

$$P_{\kappa\kappa'} = \sum_\nu |V_{\kappa\nu}^{sR}\rangle \langle V_{\kappa'\nu}^{sL}| \quad (43)$$

$$Q = I - P, \quad (44)$$

so that any matrix  $M$  can be separated into  $M^P + M^Q$  with  $M^P = PM$  and  $M^Q = QM$ .

To derive an approximate master equation for spin decay, we introduce the following ansatz -

**Ansatz I:** The steady-state Wigner function  $\rho$  consists of a dominant part  $\rho^P = P\rho$  and a small correction  $\delta = Q\rho$ , i.e.,

$$\rho(t, \mathbf{R}) = \rho^P(t, \mathbf{R}) + \delta(t, \mathbf{R}), \quad (45)$$

with  $|\delta| \ll |\rho^P|$ . Define  $S_\nu(t, \mathbf{R}) = \langle V_{\kappa\nu}^{sL} | \rho_\kappa \rangle$ , then spin evolution can be well described by  $S_\nu(t, \mathbf{R})$ .

In this work, we adopt a specific choice:

**Ansatz II:**  $V_{\kappa\alpha}^{sR} = \rho^{s_\alpha}$  and  $V_{\kappa\alpha}^{sL} = \varrho^{s_\alpha}$  with  $\alpha=x, y, z$  (see the text below Eq. 42 in Sec. II B 1).

Consequently, the linearized master equation, Eq. 5, can be written as (noting that  $L^{C,Q}\rho^P = 0$  and  $L^{C,P}\delta = 0$ )

$$\left\{ \begin{array}{l} \frac{d\rho^P}{dt} + \frac{d\delta}{dt} + \\ [L^v \cdot \nabla_{\mathbf{R}} - (L^{e,Q} + L^{E,Q})] \rho^P \\ + [L^v \cdot \nabla_{\mathbf{R}} - (L^e + L^E)] \delta \end{array} \right\} = L^P \rho^P + L^{C,Q} \delta. \quad (46)$$

To proceed to a reduced master equation of only  $S_\alpha(t, \mathbf{R})$ , we need to consider relative magnitudes of different terms in the above equation and make the following ansatz -

**Ansatz III:**  $|d\rho^P/dt|$ ,  $|L^P \rho^P|$  and the left 4th term are much smaller than  $|L^{C,Q} \delta|$  and the left 3rd term. This condition is typically satisfied in practice; the justification is provided in Appendix E.

Based on these three ansatzes, we obtain a reduced master equation of  $S_\alpha(\mathbf{R})$  (see derivation in Appendix F):

$$\frac{dS_\alpha}{dt} = D_{ij,\alpha\beta} \frac{d^2 S_\beta}{dR_i dR_j} + v_{j,\alpha\beta}^d(\mathbf{E}) \frac{dS_\beta}{dR_j} - \Gamma_{\alpha\beta}^P(\mathbf{E}) S_\beta, \quad (47)$$

where  $D_{ij}$ ,  $v_j^d(\mathbf{E})$  and  $\Gamma_\alpha^P(\mathbf{E})$  are effective diffusion-coefficient, drift-velocity and scattering-rate matrices

(with indices corresponding to spin directions). Define  $T = -(L^{C,Q})^{-1}$ , we have

$$D_{ij} = \varrho^{s,\dagger} L^{v_i} T L^{v_j} \rho^s, \quad (48)$$

$$v_j^d(\mathbf{E}) = E_j \tilde{\mu}_j + v_j^{d0}, \quad (49)$$

$$\tilde{\mu}_j = -E_j^{-1} \varrho^{s,\dagger} (L^{v_j} T L^{e,Q} + L^e T L^{v_j}) \rho^s, \quad (50)$$

$$v_j^{d0} = -\varrho^{s,\dagger} (L^{v_j} T L^{e,Q} + L^e T L^{v_j}) \rho^s, \quad (51)$$

$$\Gamma^P(\mathbf{E}) = \Gamma^0 + \Omega^t(\mathbf{E}) + \Gamma^{PE}(\mathbf{E}), \quad (52)$$

$$\Gamma^0 = \varrho^{s,\dagger} (-L^{C,P} - L^e T L^{e,Q}) \rho^s, \quad (53)$$

$$\Omega^t(\mathbf{E}) = \varrho^{s,\dagger} (L^{e,P} + L^{E,P}) \rho^s \quad (54)$$

$$- \varrho^{s,\dagger} (L^E T L^{e,Q} + L^e T L^{E,Q}) \rho^s, \quad (55)$$

$$\Gamma^E(\mathbf{E}) = -\varrho^{s,\dagger} L^E T L^{E,Q} \rho^s. \quad (56)$$

The physical interpretations of these terms are as follows:

(i) Practically,  $T$  can be well approximated as the momentum lifetime  $\tau_m$ , so that the effective diffusion coefficient  $D_{jj\alpha\alpha} \approx v_{Fjj}^2 \tau_m$  with  $v_{Fjj}^2$  being  $R_j$ -component of Fermi velocity square. In this work,  $T$  is computed by inverting  $L^C$  matrix, although using  $T \approx \tau_m$  only slightly alters the final results.

(ii)  $\tilde{\mu}_j$  is effective mobility and can be regarded as carrier mobility or its negative values for conduction electrons or holes respectively in semiconductors. According to Appendix G, we approximately have  $\tilde{\mu}_j \approx e\tau_m/\tilde{m}_j$ , with  $\tilde{m}_j^{-1} = \varrho^{\dagger}(\hbar^{-1}dv_{kj}/\hbar dk_j)\rho_s$ .

(iii)  $v_j^{d0}$  can be expressed as  $D_{jj} \Omega^{R_j}$ , where  $\Omega^{R_j}$  accounts for zero-magnetic-field spatial spin precession due to spin-orbit fields.

(iv)  $\Gamma^0$  is zero-electric-field spin relaxation rate.  $\Gamma^0$  is actually the sum of EY spin relaxation rate  $\Gamma^{EY} = -\varrho^{s,\dagger} L^{C,P} \rho^s$  and D'yakonov-Perel' (DP) spin relaxation rate  $\Gamma^{DP} = -\varrho^{s,\dagger} L^e T L^{e,Q} \rho^s \approx \tau_m \Omega^2$  with  $\Omega^2 = -\varrho^{s,\dagger} L^e T L^{e,Q} \rho^s$ . DP spin relaxation arises from random spin precession between adjacent scattering events.

(v)  $\Omega^t$  describes temporal spin precession, arising not only from an external magnetic field (Zeeman term in  $L^{e,P}$ ) and magnetic moment in magnet (via  $L^{e,P}$ ), but also from an electric-field-induced effective magnetic field (via  $L^E T L^{e,Q} + L^e T L^{E,Q}$ ).

(vi)  $\Gamma^E$  is electric-field-induced DP spin relaxation rate.

In general, the ab-mDD model (Eq. 47) does not have an explicit solution and needs to be solved numerically. For spatial homogeneous relaxation and 1D steady-state diffusion, there exists explicit solutions. See details in Appendix H.

The ab-mDD model is similar to low-order RR method (Sec. II B 1) in two aspects: (i) they both approximate the system spin dynamics using a limited number of degrees of freedom; (ii) for spin diffusion, they involve similar matrix elements. For instance, 1-RR-C (Eqs. 40-42) approximately contains  $\varrho^{s,\dagger} L^e T L^e \rho^s \approx \varrho^{s,\dagger} L^e T L^{e,Q} \rho^s$ , which also appears in the ab-mDD model if  $T$  is approximated as  $\tau_m$ . Numerically, however, they are not identical and

may show quite different results; the ab-mDD model seems often more accurate than 1-RR-C. The ab-mDD model has the advantage of clear physical interpretability, since it is a generalization of the standard drift-diffusion model with additional key effects from the terms  $v_j^{d0}$ ,  $\Omega^t$  and  $\Gamma^{PE}$ . While low-RR method has the advantage that it can be systematically improved by selecting better  $V^{R(L)}$  and increasing the order.

It is possible to derive other drift-diffusion models by decomposing  $\rho$  into more than two parts, choosing different  $V^{sR(L)}$ , or reorganizing the terms of Eq. 47 differently. However, such alternatives may encounter specific issues. For example, if we set  $V_{\kappa\alpha}^{sR(L)}$  as  $U_{s\alpha,\kappa}^{tR(L)}$  (eigenvector corresponding to  $\Gamma_{s,\alpha}^0$ ), the term  $v_j^{d0}$  in the resulting drift-diffusion model will be  $-U_s^{tL,\dagger} L^{v_j} T L^{e,Q} U_s^{tR}$ , which is approximately half of  $v_j^{d0}$  (Eq. 51) in our proposed ab-mDD model and thus underestimates the significance of zero-magnetic-field spatial spin precession.

### 3. Three model formulas of $l_s(E)$ with simple analytic expressions

Eq. 1 can be rewritten as

$$\frac{1}{l_s(E)} = \sqrt{\frac{1}{l_{s0}^2} + \frac{E^2}{4}\eta^2} - \theta \frac{|E|}{2}\eta, \quad (57)$$

where the parameter  $\eta$  is a positive constant and may be estimated in different ways, leading to different results of  $l_s(E)$ . In this work, we consider three types of  $\eta$ —denoted  $\eta_1$ ,  $\eta_2$  and  $\eta_3$ :

(1) For 1D steady-state diffusion along  $x$  direction, neglecting the terms  $v_j^{d0}$ ,  $\Omega^t$  and  $\Gamma^{PE}$ , the ab-mDD model (Sec. II B 2) reduces to:

$$D_{xx} \frac{d^2 S}{dx^2} + \tilde{\mu}_x \frac{dS}{dx} = \frac{S}{\tau_{s0}}, \quad (58)$$

which is the standard drift-diffusion model at zero magnetic field, with  $D_{xx}$  and  $\tilde{\mu}_x$  being defined by Eqs. 48 and 50.  $\tau_{s0}$  is  $\tau_s$  at  $\mathbf{E}=0$ . Using the expressions  $D_{jj\alpha\alpha} \approx v_{Fjj}^2 \tau_m$  and  $\tilde{\mu}_j \approx \tau_m/\tilde{m}_j$  given below Eq. 56 in Sec. II B 2, we define

$$\eta_1 = e / (|\tilde{m}_x| v_{Fx}^2). \quad (59)$$

For a semiconductor,  $\tilde{m}$  can be regarded as Fermi-surface-averaged effective mass or its negative values, for conduction electrons or holes respectively.

(2) Instead of using carrier diffusion coefficient, we use an effective spin diffusion coefficient  $D_s$  defined from *ab initio*  $l_{s0}$  and  $\tau_s$ — $D_s = l_{s0}^2/\tau_s$ .  $\eta$  is then

$$\eta_2 = \mu/D_s, \quad (60)$$

with  $\mu$  computed via first-principles linearized Boltzmann transport equation.[30]

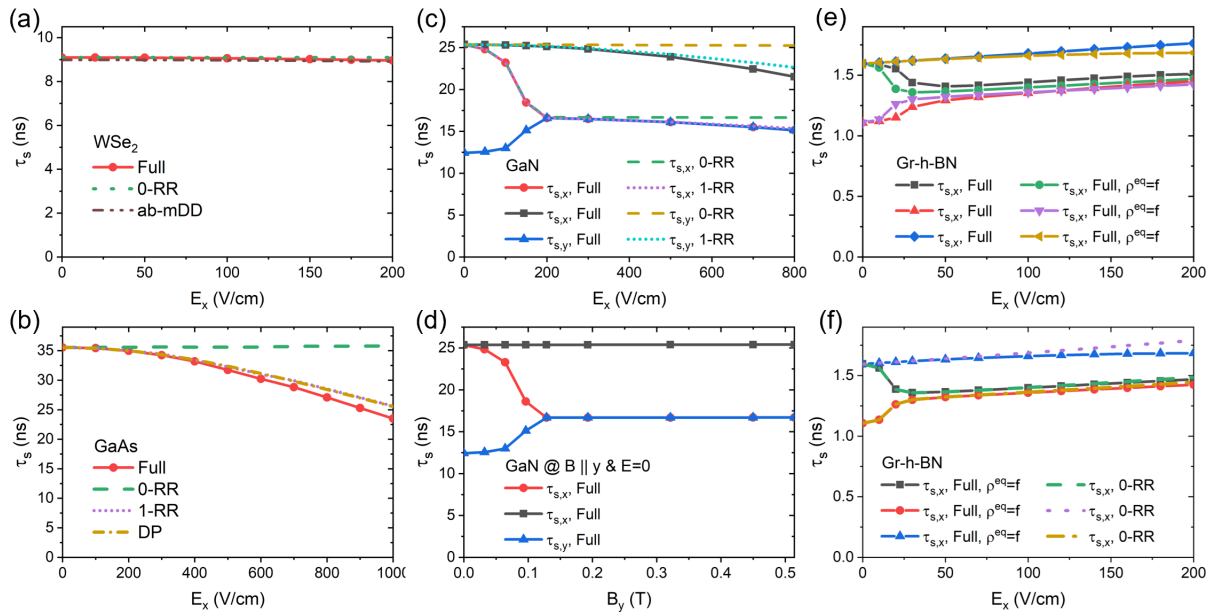


FIG. 1. Calculated electric-field ( $E_x$ ) dependent spin lifetimes ( $\tau_s(E_x)$ ) by different methods.  $\tau_s(E_x)$  of (a) holes of WSe<sub>2</sub> at 50 K, (b) electrons of GaAs at 300 K, and (c) electrons of GaN at 100 K. (d)  $\tau_s(E_x = 0)$  of GaN at different  $B_y$  (external magnetic field along  $y$ ). (e) and (f) are  $\tau_s(E_x)$  of graphene-*h*-BN at 300 K with Fermi level  $E_F=0.1$  eV. “Full” means that  $\tau_s$  is calculated by the full *ab initio* approach solving full EVP Eq. 31, with a self-consistently-computed field-dependent equilibrium density matrix  $\rho^{\text{eq}}$  (see Sec. II A 3). “*n*-RR” means that  $\tau_s(E_x)$  is computed by Eq. 36 using *n*th-order RR method considering a certain number of spin “relevant” decay modes (see Sec. II B 1). “ab-mDD” means our proposed *ab initio* matrix-drift-diffusion model (Sec. II B 2 and Eq. 47). “DP” corresponds to Eq. 62, which is a DP-like model derived from 1-RR. “Full,  $\rho^{\text{eq}}=f$ ” means that  $\tau_s$  is calculated by solving full EVP Eq. 31, but with  $\rho^{\text{eq}}$  being its zero-electric-field value - Fermi-Dirac function  $f$ .

(3) Using Einstein relation for non-degenerate semiconductors, we set  $\eta$  as

$$\eta_3 = e / (k_B T), \quad (61)$$

which was previously used in Refs. 12 and 16. The above equation can be improved by using generalized Einstein relation -  $D \approx -\mu n \frac{dn}{dE_F}$  for both degenerate and non-degenerate semiconductors. However, we find that this improvement does not change the conclusions of our study, so that we retain Eq. 61 for simplicity.

In the following, we refer to “Model 1, 2 and 3” as the models which all use Eq. 57 but with  $\eta$  being set as  $\eta_1$ ,  $\eta_2$  and  $\eta_3$  respectively.

### III. RESULTS AND DISCUSSIONS

In this work, we study  $\tau_s$  and  $l_s$  at finite  $E_x$  (electric field along  $x$  direction) for four representative systems - holes of weakly-doped (or nondegenerate) monolayer *p*-type WSe<sub>2</sub>, electrons of weakly-doped bulk *n*-type GaAs and GaN, and graphene-*h*-BN heterostructure with  $E_F=0.1$  eV. These systems are chosen to encompass different spin relaxation mechanisms, types of spin-orbit fields, and band structures. Computational details are given in Appendix I. We have not considered a metal, since the electric-field effect for metals is generally believed to be very weak[12] and our theoretical results in-

deed show that the electric-field effects on both  $\tau_s$  and  $l_s$  of Pt at 300 K are negligible even at  $E_x=10^4$  V/cm.

We focus on spin decay driven by spin-orbit coupling and the e-ph scattering, incorporating the drift dynamics due to electric fields. The electron-impurity and electron-electron scatterings are not considered for simplicity. In the main text, we present and compare results obtained from the full *ab initio* approach and various approximate methods, aiming to extract underlying physical mechanisms. The comparison between theoretical and experimental data involves multiple complexities and is discussed separately in Appendix J. The  $E_x$  range is chosen such that the maximum value of approximate  $l_s$  estimated from 0-RR simulation is about  $3l_{s0}$ . The employed quantum master equation is applicable to electric field much higher (possibly by a few orders of magnitude) than the  $E_x$  range here. But the applicability of its numerical implementation is limited by the finite-difference errors in computing  $L^E$  (Sec. II A 2). We have verified that these errors are negligible within the  $E_x$  range studied.

#### A. The electric-field effect on $\tau_s$

From Fig. 1(a), it is clear that the electric-field effect on  $\tau_s$  of WSe<sub>2</sub> is weak. Even at 1000 V/cm (not shown),  $\tau_s$  decreases by only 8%. This is expected because spins

of WSe<sub>2</sub> are highly polarized and the electric-field hardly alters the spin polarization. The slight reduction at higher electric field of 1000 V/cm likely occurs because the drift term pushes electrons toward larger wavevectors (relative to  $\pm K$ ), where spin-flip scattering is stronger. This then enhances EY spin relaxation and reduces  $\tau_s$ .  $\tau_s(E_x)$  of WSe<sub>2</sub> is well reproduced by both RR method and the ab-mDD model, confirming the validity of those approximate methods for EY systems.

In contrast,  $\tau_s$  of GaAs is strongly suppressed by an electric field, decreasing by 34% at 1000 V/cm [Fig. 1(b)]. Our theoretical results agree with earlier model calculations in Ref. 18 (Fig. 15b therein). We find that  $\tau_{sx}(E_x)$  of GaAs can be accurately described by 1-RR (1st-order RR, see Sec. II B 1) simulation and by a DP-like model derived from it. This model gives (see Appendix K)

$$\tau_{sx}^{-1}(E_x) = \tau_{sx}^{-1}(E_x = 0) + \tau \langle \Omega_{E,x}^2 \rangle, \quad (62)$$

where  $\tau$  is an effective lifetime comparable to carrier lifetime (see Appendix K). Here,  $\tau \langle \Omega_{E,x}^2 \rangle$  is interpreted as electric-field-induced DP spin relaxation rate, activated when spin precessions are present (see the end of Appendix K). Numerically,  $\langle \Omega_{E,x}^2 \rangle$  can be computed as  $\langle U_{s\alpha}^{tL} | L^E | U_{s\alpha}^{tR} \rangle$ , where  $U_{s\alpha}^{tR(L)}$  is the right (left) eigenvector of  $-L(E_x=0)$  with corresponding eigenvalue being  $\tau_{s,\alpha}^{-1}(E_x=0)$ .

We then show  $\tau_s(E_x)$  of GaN and graphene-*h*-BN in Fig. 1(c)-(f). For GaN,  $\tau_{s,x}$  and  $\tau_{s,z}$  first converge to an intermediate value as  $E_x$  rises to 200 V/cm, then decrease slowly with  $E_x$ . Whereas  $\tau_{s,y}$  decreases monotonically with  $E_x$ , similar to the GaAs. According to our prior work in Ref. 4, the  $E_x$ -dependence of  $\tau_{s,\alpha}$  ( $\alpha=x, y, z$ ) at  $E_x \leq 200$  V/cm is quite similar to the  $B_y$ -dependence ( $B_y$  is external magnetic field along  $y$  direction) of  $\tau_{s,\alpha}$  at  $E_x=0$  but finite  $B_y$ . This is confirmed by our theoretical results in Fig. 1(d). Therefore, our results indicate that the electric field induces an effective global magnetic field along  $y$  direction -  $\mathbf{B}^{E_x}$ , which is determined by spin-orbit field  $\mathbf{B}_k^{\text{soc}}$  (see Appendix L),

$$\mathbf{B}^{E_x} \approx -\frac{e}{\hbar} E_x \tau \left\langle \frac{d\mathbf{B}_k^{\text{soc}}}{dk_x} \right\rangle. \quad (63)$$

In Rashba materials including GaN and graphene-*h*-BN, the main part of  $\mathbf{B}_k^{\text{soc}}$  is  $2\alpha(k_y, -k_x, 0)$  with  $\alpha$  Rashba coefficient, so that  $\mathbf{B}^{E_x}$  is dominated by  $2e\hbar^{-1}E_x\tau\alpha(0, 1, 0)$ . Indeed, using our numerical values  $\alpha=0.018$  eV/Å and  $\tau=0.39$  ps, we find  $\mathbf{B}^{E_x} \approx 0.11$  Tesla at  $E_x=200$  V/cm, consistent with results in Fig. 1(d). Such  $\mathbf{B}^{E_x}$  causes a global Larmor precession of spin observables along  $x$  and  $z$  directions -  $S_x$  and  $S_z$ , mixing their dynamics and explaining the variations of  $\tau_{s,x}$  and  $\tau_{s,z}$  at  $E_x \leq 200$  V/cm. The behavior is well captured by the 0-RR simulation [Fig 1(c)], in which the coupled dynamics of  $S_x$  and  $S_z$  in GaN yield (complex) spin re-

laxation rates

$$\Gamma_{s\pm} \approx \frac{\Gamma_{s,x} + \Gamma_{s,z}}{2} \pm \sqrt{\frac{(\Gamma_{s,x} - \Gamma_{s,z})^2}{4} - \Omega_{xz}^2}, \quad (64)$$

with

$$\Gamma_{s,\alpha} = \tau_{s,\alpha}^{-1}(E_x = 0) - \langle U_{s\alpha}^{tL} | L^E | U_{s\alpha}^{tR} \rangle, \quad (65)$$

$$\Omega_{xz}^2 = -\langle U_{sz}^{tL} | L^E | U_{sz}^{tR} \rangle \langle U_{sx}^{tL} | L^E | U_{sz}^{tR} \rangle. \quad (66)$$

Since  $L^E$  is in principle anti-Hermitian,  $\Omega_{xz}^2$  is positive. For GaN,  $\langle U_{s\alpha}^{tL} | L^E | U_{s\alpha}^{tR} \rangle \approx 0$  and  $\Gamma_{s,\alpha} \approx \tau_{s,\alpha}^{-1}(E_x = 0)$  within the study  $E$  range. Thus, when  $E_x$  is large enough ( $\geq 200$  V/cm for GaN),  $\Omega_{xz}^2 \gg (\Gamma_{s,x} - \Gamma_{s,z})^2/4$ , we have

$$\Gamma_{s\pm} \approx \frac{\tau_{s,x}^{-1}(E_x = 0) + \tau_{s,z}^{-1}(E_x = 0)}{2} \pm i\sqrt{\Omega_{xz}^2}, \quad (67)$$

leading to two same spin lifetimes  $\tau_{s\pm} = 1/(\text{Re}\Gamma_{s\pm})$  for  $x$  and  $z$  directions.

At  $E_x > 200$  V/cm, the reduction of  $\tau_{s,\alpha}$  with  $E_x$  is however not captured by 0-RR but well described by 1-RR. This indicates such reduction arises from  $E_x$ -induced DP spin relaxation  $\tau \langle \Omega_{E,x}^2 \rangle$ .

In graphene-*h*-BN, the low-field ( $E_x \leq 300$  V/cm) behavior of  $\tau_{s,\alpha}$  resembles that of GaN:  $\tau_{s,x}$  and  $\tau_{s,z}$  first decreases and increases, respectively, then both vary slowly, whereas  $\tau_{s,y}$  changes only gradually [Fig. 1(e)]. This again reflects the presence of a finite  $\mathbf{B}^{E_x}$  along  $y$  in this Rashba system.

Two notable differences appear in graphene-*h*-BN compared with GaN. First, the electric-field-induced change of  $\tau_{s,\alpha}$  arise not only from the explicit drift term in the master equation, but also from the electric-field modification of  $\rho^{\text{eq}}$ , away from Fermi-Dirac function  $f$  [Fig. 1(e)]. Second,  $\tau_{s,x}$  and  $\tau_{s,z}$  remain distinct over the whole  $E$  range and both slowly increase at higher  $E_x$ . As  $\tau_{s,\alpha}(E_x)$  of graphene-*h*-BN are accurately described by 0-RR simulations [Fig. 1(f)] and Eqs. 64-66, this fact can be explained as: in graphene-*h*-BN,  $\langle U_{s\alpha}^{tL} | L^E | U_{s\alpha}^{tR} \rangle$  are complex values of small positive real parts and significant imaginary part at higher  $E_x$ , which makes the  $E_x$  effect very different from a pure  $B_y$ -field effect. The positive real parts of  $\langle U_{s\alpha}^{tL} | L^E | U_{s\alpha}^{tR} \rangle$  can slightly increase spin lifetimes, according to Eq. 65. Numerically,  $(\Gamma_{s,x} - \Gamma_{s,z})^2/4$  is comparable to  $\Omega_{xz}^2$  within the studied  $E$  range, so that the real part of  $\sqrt{(\Gamma_{s,x} - \Gamma_{s,z})^2/4 - \Omega_{xz}^2}$  becomes non-negligible and  $\text{Re}\Gamma_{s+} \neq \text{Re}\Gamma_{s-}$ , leading to two different spin lifetimes for  $x$  and  $z$  directions.

We further compare results of GaAs, GaN and graphene-*h*-BN by solving full EVP and the ab-mDD model in Fig. 2. The model works well for GaN but yields a few percent errors for GaAs and significant errors (up to 28%) for graphene-*h*-BN. From theoretical results of GaAs and graphene-*h*-BN in Figs. 1 and 2, the ab-mDD model appears worse than 1-RR simulation. This indicates that 1-RR simulation with  $V^{R(L)}$  set as Eq. 35 probably approximates the  $\rho$  solution more accurately

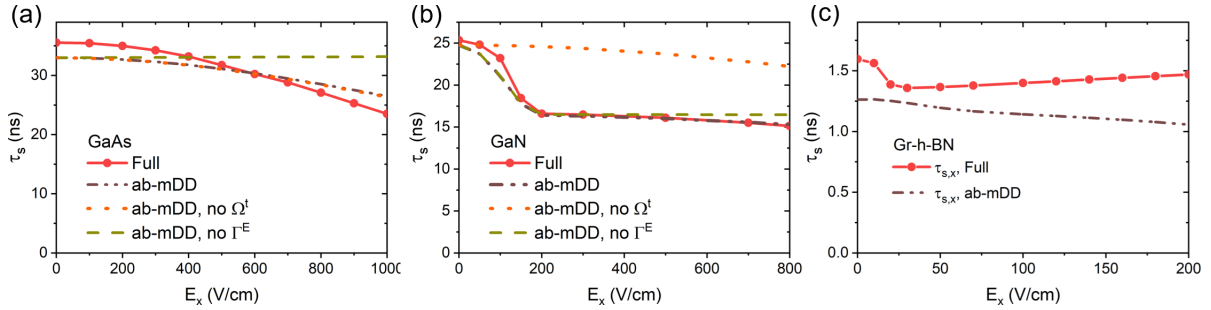


FIG. 2. Calculated  $\tau_s(E_x)$  of GaAs, GaN and graphene-*h*-BN by solving full EVP and the ab-mDD model. “no  $\Gamma^E$ ” or “no  $\Omega^t$ ” means that the  $\Gamma^E$  (Eq. 56) or  $\Omega^t$  (Eq. 54) term of the model is not considered, respectively.

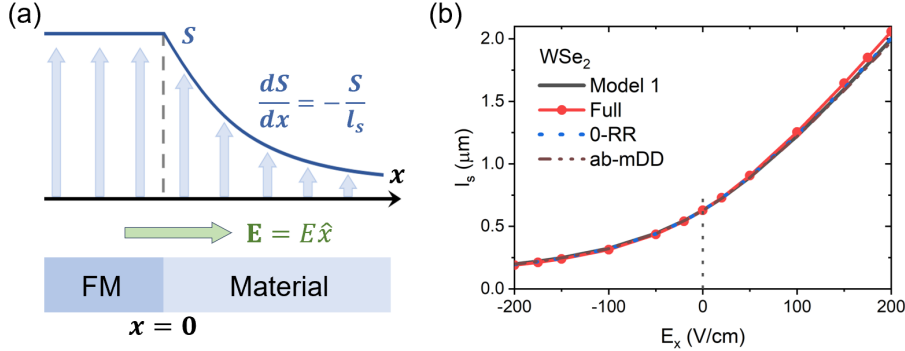


FIG. 3. (a) Schematic of the spin-diffusion setup. Spins are injected from a ferromagnet (FM) at  $x < 0$  through a transparent interface into the material at  $x \geq 0$ , where they diffuse under zero or finite  $\mathbf{E}$  along  $x$  axis. (b)  $E_x$  dependent spin diffusion length ( $l_s(E_x)$ ) of holes of monolayer WSe<sub>2</sub> at 50 K by different methods. “Model 1” uses the analytical formula Eq. 57 with  $\eta$  being  $\eta_1=e/(v_{F_x}^2 \tilde{m}_x)$  (Eq. 59). “Full” means that  $l_s$  is calculated by solving full EVP Eq. 32. “n-RR” means that  $l_s(E_x)$  is computed by solving the reduced EVP Eq. 36 using  $n$ th-order RR method with basis functions  $V^{R(L)}$  given by Eq. 37 (see Sec. II B 1).

than the ab-mDD model, which is expected as 1-RR is exact at  $\mathbf{E}=0$ .

Moreover, as discussed in Sec. II B 1, the  $\Gamma^E$  (Eq. 56) and  $\Omega^t$  (Eq. 54) terms in the ab-mDD model represent the electric-field-induced DP spin relaxation rate and temporal spin precession, respectively. Therefore, from the comparison between the ab-mDD model and the version without the  $\Gamma^E$  or  $\Omega^t$  term in Fig. 2(a)-(b), we conclude that: (i) the  $\tau_s$  reductions for GaAs and for GaN at  $E_x > 200$  V/cm are both caused by the electric-field-induced DP spin relaxation; (ii) the  $\tau_s$  variation for GaN at  $E_x \leq 200$  V/cm is attributed to the electric-field-induced temporal spin precession; and (iii) the  $\Omega^t$  term has no effect on  $\tau_s(E_x)$  of GaAs, likely because the spin-orbit fields in GaAs are primarily of cubic-Dresselhaus type, yielding  $\mathbf{B}^{E_x} \approx 0$  and hence no global field-induced spin precession. These conclusions are fully consistent with the analysis based on the 0-RR and 1-RR simulations above.

## B. The electric-field effect on $l_s$

We investigate the steady-state spin diffusion along  $x$  direction, as illustrated in Fig. 3(a). Spins are injected from a ferromagnet at  $x < 0$  to the semi-infinite material at  $x \geq 0$  and diffuses in it.

Fig. 3(b) shows calculated  $l_s(E_x)$  of WSe<sub>2</sub> holes. For holes,  $E_x > 0$  and  $E_x < 0$  correspond to downstream and upstream fields respectively. While for electrons, the situation is reversed. Thus, it is clear that  $l_s(E_x)$  values of WSe<sub>2</sub> are significantly enhanced or suppressed by moderate downstream or upstream fields respectively, as expected by the model formula Eq. 57. By comparing results by different methods, we find that “Model 1” (Eq. 57 with  $\eta=\eta_1=e/(v_{F_x}^2 \tilde{m}_x)$  from Eq. 59), 0-RR simulation (Eqs. 36-37) and the ab-mDD model all agree well with the full *ab initio* results [lines labeled as “Full” in Fig. 3(b)]. “Model 2 and 3”, using Eq. 57 but with  $\eta$  being  $\eta_2=\mu/D_s$  (Eq. 60) and  $\eta_3=e/(k_B T)$  (Eq. 61), respectively, also yield accurate results (not shown) for these materials. For EY systems such as WSe<sub>2</sub>, it has been expected that their spin diffusions are well described by the standard drift-diffusion model.[2] Here, this is confirmed by our full *ab initio* and approximate simulations.

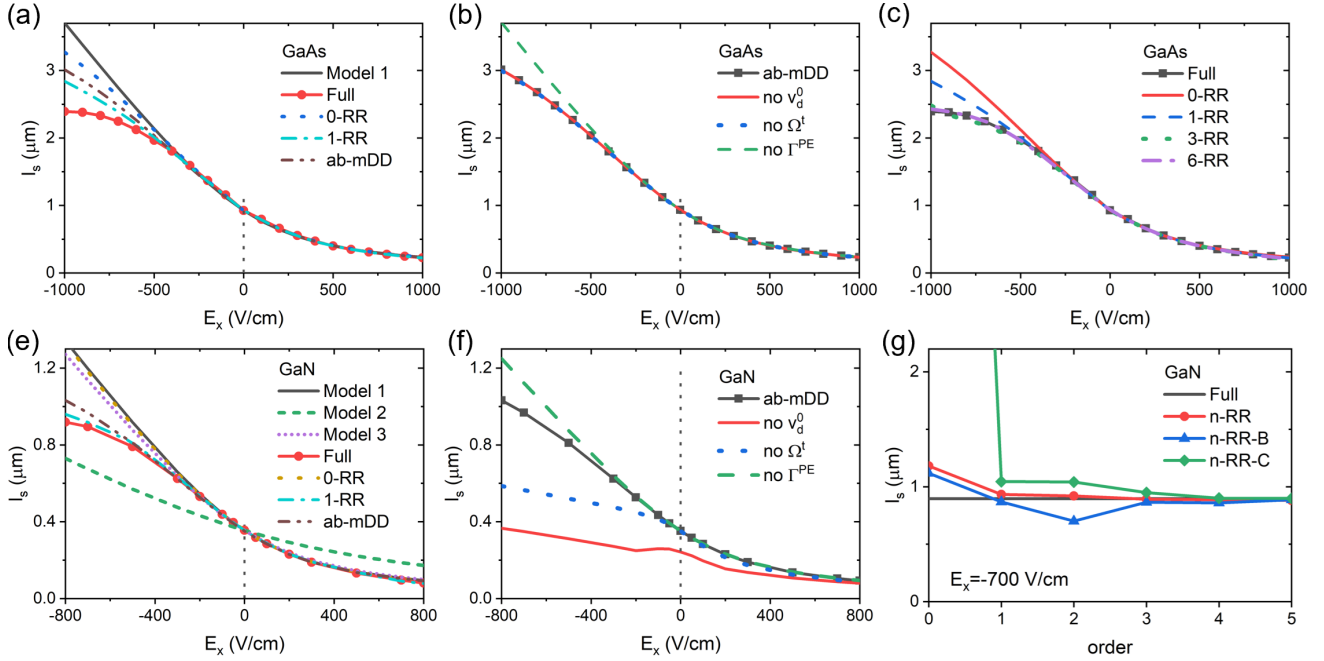


FIG. 4.  $l_s(E_x)$  of bulk GaAs at 300 K and bulk GaN at 100 K, computed by different methods. Panel (g) shows  $l_s$  of GaN at  $E_x = -700$  V/cm computed by RR methods of different orders ( $n$ ) and with different types of basis functions  $V^{R(L)}$ , compared with results by solving full EVP. “Model 1, 2 and 3” refer to the model  $l_s(E_x)$  formula Eq. 57 with the parameter  $\eta$  set as  $\eta_1$ ,  $\eta_2 = \mu/D_s$  and  $\eta_3 = e/(k_B T)$  (Eqs. 59-61), respectively. “no  $v_d^0$ ” corresponds to the ab-mDD model without the  $v_d^0$  term (Eq. 51).  $V^{R(L)}$  of  $n$ -RR,  $n$ -RR-B and  $n$ -RR-C are given in Eqs. 37, 38 and 40, respectively.

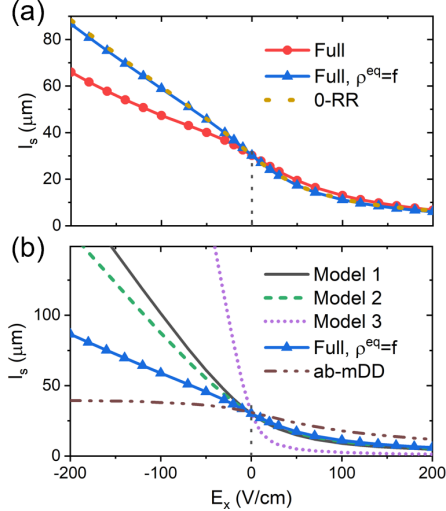


FIG. 5.  $l_s(E_x)$  of graphene-*h*-BN at 300 K, computed by different methods.

Next, we examine  $l_s(E_x)$  of two typical DP systems - conduction electrons of GaAs and GaN in Fig. 4. The full *ab initio* results [red solid lines in Fig. 4(a) and (d)] show that, as in WSe<sub>2</sub>, a moderate downstream (upstream) field strongly enhances (suppresses)  $l_s$ . However, the  $l_s$  variation with  $E_x$  weakens at  $E_x \leq -500$  V/cm. At  $E_x \geq -400$  V/cm, all approximate methods except “Model 2” reproduce the full *ab initio* results well. However,

at  $E_x \leq -500$  V/cm, “Model 1-3” and 0-RR simulation all exhibit significant errors. The ab-mDD model and 1-RR simulations substantially improve theoretical results. The improvement is partly because of the inclusion of the electric-field-induced DP spin relaxation, as discussed above. Overall, 1-RR simulation performs best, but it still has non-negligible errors at  $E_x \leq -800$  V/cm for GaAs. Such errors can be reduced by using higher-order RR simulations, as demonstrated in Fig. 4(c). Our results indicate that for certain materials at high downstream electric field, the  $\rho$  solution for spin diffusion may not be accurately expressed by relatively simple forms assumed in the ab-mDD model (Eq. 45), 0-RR and 1-RR simulations (Eq. 37); instead, a more complete basis set provided by a higher-order RR simulation is required.

In Fig. 4(b) and (f), we show  $l_s(E_x)$  of GaAs and GaN by the ab-mDD model and the version without the  $v_d^0$ ,  $\Omega^t$  or  $\Gamma^E$  term. For both GaAs and GaN, the  $\Gamma^E$  term, corresponding to electric-field-induced DP spin relaxation, reduces  $l_s$  at high downstream electric field. The  $\Omega^t$  term (corresponding to field-induced temporal spin precession) has no effect on  $l_s(E_x)$  of GaAs but a significant effect on  $l_s(E_x)$  of GaN, similar to  $\tau_s(E_x)$  of them. The  $v_d^0$  term, corresponding to the zero-field spatial spin precession, strongly affects  $l_s(E_x)$  of GaN in the whole  $E_x$  range. The importance of zero-field spatial spin precession on spin diffusion has been observed in previous theoretical and experimental studies.[2, 4, 14] The effects of  $v_d^0$ ,  $\Omega^t$  and  $\Gamma^E$  terms are not considered in the simple model for-

mula Eq. 57, which explains the large errors of “Model 1-3”.

We compare  $l_s$  of GaN at  $E_x = -700$  V/cm by  $n$ -RR,  $n$ -RR-B and  $n$ -RR-C simulations with different  $n$  in Fig. 4(f).  $n$ -RR,  $n$ -RR-B and  $n$ -RR-C use different basis sets and set  $V^{R(L)}$  as Eqs. 37, 38 and 40, respectively (Sec. II B 1). Among them,  $n$ -RR is the most accurate, as expected because  $n$ -RR is exact at  $E_x = 0$ . Notably, 0-RR-C fails completely, while 1-RR-C yields much more reasonable result. This fact is also observed for two other DP systems - GaAs and graphene-*h*-BN (not shown). On the other hand, 0-RR-C gives reasonable results for a EY system - WSe<sub>2</sub>. For WSe<sub>2</sub> (at 50 K) at  $E_x = 0$  and 200 V/cm,  $l_s$  by 0-RR-C simulation is 0.58 and 1.7  $\mu\text{m}$  respectively, not very far from 0.62 and 2  $\mu\text{m}$  by solving full EVP. Therefore, while 0-RR-C may work in some EY systems, it fails in DP systems. This probably indicates that for spin diffusion in DP systems, the basis functions of 0-RR-C lack essential components of the true solution of  $\rho$ , so that it is necessary to introduce more basis functions via higher-order RR-C. Overall, our results indicate that the choice of trial vectors  $V^{R(L)}$  is critical to RR simulations and higher-order RR simulations generally improve accuracy.

We further show  $l_s(E_x)$  of graphene-*h*-BN at 300 K in Fig. 5.  $E_F$  is set as 0.1 eV to ensure free carriers are dominated by conduction electrons, so that spin-drift effect from electrons is not reduced by that from holes. As for  $\tau_s(E_x)$  of graphene-*h*-BN, the electric-field-induced change of  $l_s$  arise not only from the explicit drift term in the master equation, but is also significantly affected by the electric-field modification of  $\rho^{\text{eq}}$ . This effect, not observed in WSe<sub>2</sub>, GaAs or GaN, further enhances the discrepancy between the full *ab initio* results and those by approximate methods in graphene-*h*-BN, since this effect modifies the scattering term and cannot be directly considered in approximate methods.

0-RR simulation is found in perfect agreement with the full *ab initio* simulation for  $l_s(E_x)$ , just as it did for  $\tau_s(E)$  of graphene-*h*-BN. This indicates that the electric-field-induced DP spin relaxation (present in 1-RR but not in 0-RR) is absent in graphene-*h*-BN within the studied  $E_x$  range. As shown in Fig. 5(b), the ab-mDD model and “Model 1-3” all fail to simulate  $l_s(E_x)$  correctly. “Model 3” performs worst, since it relies on Einstein relation valid only in non-degenerate semiconductors with parabolic bands. The failure of the ab-mDD model is not surprising, since it already fail to simulate  $\tau_s(E_x)$  of graphene-*h*-BN. Our results suggest that certain important components of the actual  $\rho$  solution are correctly included in 0-RR simulation but not in the ab-mDD model. While the ab-mDD model may be refined—for example, by decomposing  $\rho$  into more than two components—developing a simple yet universally accurate model is non-trivial and lies beyond the scope of this work.

Moreover, our numerical tests show that the failure of “Model 1-3” and the ab-mDD model persists in graphene-*h*-BN when an external magnetic field is

applied,  $E_F$  is shifted to 0.05 eV, or the strength of spin-orbit field, scattering, or intervalley scattering is rescaled (by a factor from 0.25 to 4). We have observed that under particular sets of conditions, “Model 2” yields  $l_s(E_x)$  values within 10 % of the full *ab initio* results. However, under the same conditions, “Model 1 and 3” and the ab-mDD model still exhibit significant errors  $\geq 20\%$ . Furthermore, even this limited agreement with “Model 2” disappears if the SOC or scattering strength is altered further, or if external conditions are modified (for example, by applying a magnetic field). These observations suggest that the apparent agreement of “Model 2” is likely coincidental. In conclusion, the drift-diffusion model generally does not work properly in pristine graphene-*h*-BN. A more detailed microscopic analysis—potentially combined with model-Hamiltonian studies—will be needed to fully understand the reasons for this systematic failure, a task we leave for future work.

Overall, our theoretical results indicate that the simple model formulas (“Model 1-3”) can cause significant errors of  $l_s(E_x)$  at moderate  $E_x$ . More sophisticated approximate methods, including the ab-mDD model, 0-RR and 1-RR simulations, typically improve the results but may still yield significant errors for certain materials and/or conditions. Therefore, accurate simulations based on the full *ab initio* approach are critical to the correct prediction and understanding of the electric-field effect on  $l_s$  in general cases.

Finally, to provide a clear overview of the accuracy of different approximate methods, Table I summarizes their relative errors in estimating  $\tau_s(E_x)$  and  $l_s(E_x)$  at selected downstream electric fields for each studied system, along with relevant system information.

#### IV. SUMMARY AND OUTLOOKS

In summary, we implement the drift term due to finite  $\mathbf{E}$  within our *ab initio* approach of  $l_s$ , based on a linearized density-matrix master equation. Our method is applied to study the electric-field effect on  $\tau_s$  and  $l_s$  in several representative materials. We compare theoretical results by the full *ab initio* approach with several approximate methods, including low-order RR method, our proposed ab-mDD model and a few simple model formulas using Eq. 57 from the standard drift-diffusion model. We find that although those approximate methods perform well in WSe<sub>2</sub>, they may cause significant errors for certain materials at moderate  $E_x$ , which highlights the importance of carrying out full *ab initio* simulations. The detailed theoretical analysis reveal the importance of a DP-type spin relaxation (Eq. 62) and a global temporal spin precession due to  $B^E$  (Eq. 63), both induced by periodic-direction electric-field, to  $\tau_s(E)$  and  $l_s(E)$ . The effect of zero-magnetic-field spatial spin precession, corresponding to the  $v_d^0$  term in the ab-mDD model, is also found critical to  $l_s(E)$  of both GaN and graphene-*h*-BN. We also find that the electric-field modification of  $\rho^{\text{eq}}$

	System	$\tau_s$ type	SOC fields	Relative error of method at $ E_x^{\text{down}} =E_{\text{max}}$ ( $0.5E_{\text{max}}$ ; 0)			
				“Model 1”	ab-mDD	0-RR	1-RR
$\tau_s$	WSe <sub>2</sub>	EY	–	–	1% (1%; 1%)	1% (0%)	–
	GaAs	DP	Dresselhaus	–	<b>13%</b> (2%; 7%)	<b>52%</b> (12%)	9% (2%)
	GaN	DP	Rashba	–	1% (1%; 2%)	10% (2%)	1% (0%)
	Gr-BN	DP	Rashba	–	<b>28%</b> ( <b>18%</b> ; <b>21%</b> )	1% (0%)	–
$l_s$	WSe <sub>2</sub>	EY	–	0% (0%)	1% (1%; 0%)	0% (0%)	–
	GaAs	DP	Dresselhaus	<b>55%</b> (9%)	<b>26%</b> (4%; 1%)	<b>37%</b> (8%)	<b>19%</b> (2%)
	GaN	DP	Rashba	<b>46%</b> (10%)	<b>12%</b> (1%; 1%)	<b>45%</b> (9%)	5% (2%)
	Gr-BN	DP	Rashba	<b>119%</b> ( <b>72%</b> )	<b>55%</b> ( <b>35%</b> ; 3%)	2% (1%)	–

TABLE I. Relative errors of approximate methods compared with the full *ab initio* approach at selected downstream electric fields  $E_x^{\text{down}}$  for  $\tau_s(E_x)$  and  $l_s(E_x)$  of different systems, with relevant system information. Gr-BN means graphene-*h*-BN. “ $\tau_s$  type” indicates type or mechanism of spin relaxation. For each system,  $E_{\text{max}}$  is the maximum studied  $E_x$  of this system. The value outside brackets is relative error at  $|E_x^{\text{down}}|=E_{\text{max}}$ . The first number in brackets corresponds to  $|E_x^{\text{down}}|=0.5E_{\text{max}}$ . The second number (if present) in brackets corresponds to  $E_x=0$ . Errors exceeding 10% are highlighted. By construction,  $l_{s0}$  by “Model 1” and  $n$ -RR simulations are exactly the full *ab initio*  $l_{s0}$  at  $E_x=0$ ; therefore, their corresponding errors at  $E_x=0$  are omitted. Relative errors of “Model 2 and 3” are not shown, since they are either similar to or larger than those of “Model 1”.

can significantly affect  $\tau_s(E)$  and  $l_s(E)$ , an effect absent in previous theoretical studies.

Our *ab initio* framework with finite  $\mathbf{E}$  may be further extended to simulate other linear or nonlinear carrier and spin transport properties, with quantum treatment of electron scattering processes and the inherent inclusion of Berry phase effects. In the present work, the scattering term does not explicitly include  $\mathbf{E}$ , which is however an approximation. A more complete theory would require reformulating the density-matrix master equation to fully account for the field dependence of scattering, for instance, by adopting a phonon-assisted density matrix formalism[31]. This extension, however, would introduce considerable complexity, notably through the appearance of covariant derivatives of the e-ph matrix elements. Given the considerable technical challenges involved and the expectation that this contribution is weaker than the electric-field effect due to the drift term, we defer the treatment of field-dependent scattering to future work.

## ACKNOWLEDGMENTS

This work is supported by National Natural Science Foundation of China (Grant No. 12574257 and 12304214), Fundamental Research Funds for Central Universities (Grant No. JZ2023HGPA0291 and JZ2025HGQA0310). This research used resources of the HPC Platform of Hefei University of Technology.

## APPENDICES

### Appendix A: $L^{v_j}$ and $L^e$ in linearized master equation

$L^{v_j}$  and  $L^e$  are

$$L_{kab,k'cd}^{v_j} = \frac{1}{2} (v_{j,kac} \delta_{bd} + \delta_{ac} v_{j,kdb}) \delta_{kk'}, \quad (68)$$

$$L_{kab,k'cd}^e = \frac{-i}{\hbar} (H_{kac}^e \delta_{bd} - \delta_{ac} H_{kdb}^e) \delta_{kk'}. \quad (69)$$

### Appendix B: Comparisons with standard Boltzmann transport equation (BTE) and kinetic spin Bloch equation (KSBE)

Quantum master equation can be viewed as a generalization of standard BTE and is reduced to BTE by replacing  $\rho_{kab}$  to its diagonal part  $\rho_{ka}^d = \rho_{kab} \delta_{ab}$ . Define  $P_{ka,k'b}^d = P_{kab,k'bb}$ , the resulting scattering term  $C[\rho^{\text{tot},d}]$  reads

$$C_{ka}[\rho^{\text{tot},d}] = (1 - \rho_{ka}^{\text{tot},d}) P_{ka,k'b}^d \rho_{k'b}^{\text{tot},d} - \rho_{ka}^{\text{tot},d} P_{ka,k'b}^d (1 - \rho_{k'b}^{\text{tot},d}), \quad (70)$$

which is derived using the property of  $P_{ka,k'b}^d = P_{k'b,ka}^d$  and all  $P^d$  elements are real values.  $P_{ka,k'b}^d$  is actually the e-ph transition rate between electron states  $\{k, a\}$  and  $\{k', b\}$ .

The linearized scattering term  $L^{Cd}$  reads

$$L_{ka,k'b}^{Cd} = - P_{ka,k'b}^d (\rho_{ka}^d - \rho_{k'b}^d), \quad (71)$$

which has been commonly employed in theoretical simulations based on standard BTE.

A critical difference between quantum master equation and standard BTE is that Larmor spin precession is not directly included in standard BTE.

Standard KSBE is an alternative form of quantum master equation for two-band systems. Within standard KSBE, the  $2 \times 2 \rho$  is expressed as

$$\rho_k = \frac{\tilde{n}_k}{2} I + \tilde{s}_{k\alpha} \sigma_\alpha, \quad (72)$$

where  $\tilde{n}_k = \rho_{k11} + \rho_{k22}$ ,  $\tilde{s}_{kx} = \text{Re} \rho_{k12}$ ,  $\tilde{s}_{ky} = -\text{Im} \rho_{k12}$  and  $\tilde{s}_{kz} = (\rho_{k11} - \rho_{k22})/2$ .

In principle, standard KSBE and quantum master equation are equivalent for two-band systems. Nevertheless, our used quantum master equation is more general, as it applies to arbitrary band structures. Moreover, practical forms of KSBE in the literature may employ additional approximations. For instance, the energy-conservation-related function in the scattering term may use electron energies without considering the modifications due to spin-orbit fields. This is usually a minor assumption but may cause some errors if spin-orbit fields are very strong. Additionally, previous KSBE simulations relied on model Hamiltonian and highly-simplified treatment of the scattering term, these limitations are removed in our *ab initio* quantum-master-equation simulations.

### Appendix C: Spin perturbative density-matrix $\rho^{s_\alpha}$

$\rho^{s_\alpha}$  reads

$$\rho_{kab}^{s_\alpha} = c^\rho \left( \frac{\Delta f}{\Delta \epsilon} \right)_{kab} s_{\alpha, kab}, \quad (73)$$

$$\left( \frac{\Delta f}{\Delta \epsilon} \right)_{kab} = \left( \frac{df}{d\epsilon} \right)_{kab} \delta_{\epsilon_{ka} \epsilon_{kb}} + \frac{f_{ka} - f_{kb}}{\epsilon_{ka} - \epsilon_{kb}} (1 - \delta_{\epsilon_{ka} \epsilon_{kb}}), \quad (74)$$

where  $c^\rho$  is an arbitrary constant.

### Appendix D: The computation of the observable evolution and the evaluation of $\tau_s$ and $l_s$

Having the observable operator  $o_\kappa$ , and defining  $o_\mu^t = N_k^{-1} \sum_\kappa o_\kappa^* U_{\kappa\mu}^{tR}$  and  $o_\nu^x = N_k^{-1} \sum_\kappa o_\kappa^* U_{\kappa\nu}^{xR}$ , the observable evolution for relaxation problem is:[4]

$$O(t) = \text{Re}(\Sigma_\mu c_\mu^t o_\mu^t e^{-\Gamma_\mu t}), \quad (75)$$

and for diffusion problem is:

$$O(x) = \text{Re}(\Sigma_\nu c_\nu^x o_\nu^x e^{-\lambda_\nu^x x}). \quad (76)$$

Eq. 75 and 76 accurately describes the observable decay for given  $\rho^{\text{pert}}$ . The observable dynamics consist of dynamics of individual decay modes, highly simplifying the analysis compared to previous real-time

method[32, 33]. For given  $\rho^{\text{pert}}$  and  $o$ , the relevance of a mode to  $O(t)$  or  $O(x)$  is determined by its eigenvectors and can be measured by the corresponding mode-resolved normalized relevance factor

$$\mathcal{R}_\mu^{t(x)} = \frac{\left| c_\mu^{t(x)} o_\mu^{t(x)} \right|}{\max_{\mu'} \left\{ \left| c_{\mu'}^{t(x)} o_{\mu'}^{t(x)} \right| \right\}}. \quad (77)$$

For slow decay of spin observable, typically only a few modes are relevant, so that  $O(t)$  or  $O(x)$  is well described by eigenvalues and eigenvectors of these “relevant” modes. If only one mode  $\mu_0$  is relevant, diffusion length along  $x$  direction -  $l^x$  (lifetime  $\tau$ ) for the observable is simply  $l^x(\tau)$  of this  $\mu_0$  mode. With multiple non-degenerate relevant modes, to describe the observable decay by a single  $l^x(\tau)$  value, we need to define an effective or averaged diffusion length  $\bar{l}^x$  (lifetime  $\bar{\tau}$ ) length as

$$\bar{\tau} = \frac{\sum_{\mu \in \mu^{\text{rel}}} \mathcal{R}_\mu^t \tau_\mu}{\sum_{\mu \in \mu^{\text{rel}}} \mathcal{R}_\mu^t}, \quad (78)$$

$$\bar{l}^x = \frac{\sum_{\nu \in \nu^{\text{rel}}} \mathcal{R}_\nu^x l_\nu^x}{\sum_{\nu \in \nu^{\text{rel}}} \mathcal{R}_\nu^x}, \quad (79)$$

where  $\mu^{\text{rel}}$  ( $\nu^{\text{rel}}$ ) includes the “relevant” modes with  $\mathcal{R}_\mu^t \geq 0.1$  ( $\mathcal{R}_\nu^x \geq 0.1$ ). In this work, for  $s_x$  spin perturbation and  $s_x$  observable operator,  $\mu^{\text{rel}}$  ( $\nu^{\text{rel}}$ ) includes either one or two modes.

### Appendix E: About Ansatz III for the ab-mDD model

The reasons why Ansatz III for Eq. 46 typically holds are:

First, for  $L^P \rho^P = (L^C + L^{e,P} + L^{E,P}) \rho^P$ , we have  $|L^C \rho^P| \approx \Gamma_\alpha^{\text{EY}} |\rho^P|$ . Both  $L^{e,P}$  and  $L^{E,P}$  are approximately anti-Hermitian matrices, so that  $|(L^{e,P} + L^{E,P}) \rho^P| \approx |\Omega| |\rho^P|$  with  $\Omega$  being an effective Larmor precession frequency. As  $\Gamma_\alpha^s$  and  $|\Omega|$  are typically tiny,  $|L^P \rho^P|$  is tiny and much smaller than  $|L^{C,Q} \delta|$  and the left 3rd term.  $d\rho^P/dt$  should have similar magnitude to  $L^P \rho^P$  and therefore likewise tiny.

Second,  $L^{C,Q} \delta \approx \tau_m^{-1} |\rho^P|$  with  $\tau_m$  being momentum lifetime. Typically,  $\tau_m^{-1}$  is relatively larger, considering that  $\delta \ll \rho_\kappa^P$ , we can safely assume that the left 4th term is much smaller than  $|L^{C,Q} \delta|$  and the left 3rd term.

### Appendix F: The derivation of Eq. 47

From Ansatz III for the ab-mDD model, we obtain the following two equations:

$$[L^v \cdot \nabla_R - (L^{e,Q} + L^{E,Q})] \rho^P \approx L^{C,Q} \delta, \quad (80)$$

$$\frac{d\rho^P}{dt} + [L^v \cdot \nabla_R - (L^e + L^E)] \delta \approx L^P \rho^P. \quad (81)$$

From Eq. 80,

$$\delta \approx (L^{C,Q})^{-1} [L^v \cdot \nabla_R - (L^{e,Q} + L^{E,Q})] \rho^P. \quad (82)$$

Insert it into Eq. 81 and multiply  $\varrho^{s,\dagger}$  to the left, we obtain Eq. 47.

#### Appendix G: The approximate formula of effective mobility $\tilde{\mu}_j$ in Eq. 50 of the ab-mDD model

Suppose spins are highly polarized along  $\alpha$  direction or there are two Kramers degenerate bands with one spin-up and the other spin-down. In these cases, spin matrix (in Bloch basis)  $s_\alpha$  is approximately  $k$ -independent. Therefore, we have

$$\rho_k^{s_\alpha} = c^\rho \frac{df_k}{d\epsilon} s_\alpha, \quad (83)$$

We also suppose  $\varrho^{s_\alpha} = c^\varrho s_\alpha$ .  $c^\rho$  and  $c^\varrho$  are real constants and their choices must satisfy  $\varrho^{s_\alpha} \rho^{s_\alpha} = 1$ .

Approximate  $T$  as momentum lifetime  $\tau_m$ , we have

$$\tilde{\mu}_j \approx -\tau_m E_j^{-1} \varrho^{s_\alpha} (L^{v_j} L^{E,Q} + L^E L^{v_j}) \rho^{s_\alpha}. \quad (84)$$

Suppose  $\xi$ -part of  $L^E$  is negligible, which is satisfied in one-band systems and in many systems if smooth basis functions are chosen. Thus, we can approximate  $L^E \approx \frac{eE_j}{\hbar} \frac{d}{dk_j}$ . Therefore, considering that  $L^{E,Q} \approx L^E$ , we have

$$\begin{aligned} E_j^{-1} \varrho^{s_\alpha} L^{v_j} L^E \rho^{s_\alpha} &= \frac{e}{\hbar} c^\varrho c^\rho \text{Tr}(s_\alpha^2) \int_\Omega d\mathbf{k} v_{kj} \frac{d}{dk_j} \frac{df_k}{d\epsilon} \\ &= -\frac{e}{\hbar} c^\varrho c^\rho \int_\Omega d\mathbf{k} \frac{df_k}{d\epsilon} \frac{d}{dk_j} v_{kj} \\ &= -e \varrho_s^\dagger \frac{dv_{kj}}{\hbar dk_j} \rho_s, \end{aligned} \quad (85)$$

$$\begin{aligned} E_j^{-1} \varrho^{s_\alpha} L^E L^{v_j} \rho^{s_\alpha} &= 2 \frac{e}{\hbar} c^\varrho c^\rho \int_\Omega d\mathbf{k} \frac{d}{dk_j} \left( v_{kj} \frac{df_k}{d\epsilon} \right) \\ &= 0. \end{aligned} \quad (86)$$

Define

$$\tilde{m}^{-1} = \varrho_s^\dagger \frac{dv_{kx}}{\hbar dk_x} \rho_s, \quad (87)$$

we then have

$$\tilde{\mu} \approx e\tau_m / \tilde{m}. \quad (88)$$

#### Appendix H: The solution for 1D steady-state diffusion within the ab-mDD model

For 1D steady-state diffusion along  $x$  direction and assuming  $\mathbf{E} \parallel x$ , we have

$$D_{xx} \frac{d^2 S}{dx^2} + v_x^d \frac{dS}{dx} = \Gamma^P S. \quad (89)$$

The general solution is

$$S(x) = Y^R e^{-\lambda x} c^x, \quad (90)$$

with  $\lambda$  and  $Y^R$  satisfy

$$D_{xx} Y^R \lambda^2 - v_x^d Y^R \lambda = \Gamma^P Y^R. \quad (91)$$

This is quadratic eigenproblem. Define  $Z^R = (Y^R, \lambda Y^R)$ , we have the standard eigenproblem for  $\lambda$ :

$$A^Z Z^R = Z^R \lambda, \quad (92)$$

$$\begin{aligned} A^Z &= \begin{pmatrix} I & 0 \\ 0 & D_{xx}^{-1} \end{pmatrix} \begin{pmatrix} 0 & I \\ \Gamma^P & v_x^d \end{pmatrix} \\ &= \begin{pmatrix} 0 & I \\ D_{xx}^{-1} \Gamma^P & D_{xx}^{-1} v_x^d \end{pmatrix}. \end{aligned} \quad (93)$$

For 1D diffusion at  $x \geq 0$  with the boundary conditions:

$$S(0) = S_0, \quad (94)$$

$$S(+\infty) = 0, \quad (95)$$

where  $S_0$  can be determined by maximum the spin observable. Then, we have

$$c^x = Y^{R,-1} S_0,$$

and

$$S_m(x) = \sum_{\lambda_\mu > 0, \kappa'} Y_{m\mu}^R e^{-\lambda_\mu x} (Y^{R,-1})_{\mu n} S_{0,n}. \quad (96)$$

If  $V^{sR}$  has only one column and is highly relevant to spin, then  $A^Z$  is  $2 \times 2$  matrix. Assuming  $\Gamma^P = \tau_{s0}^{-1}$ , the eigenvalues are

$$\begin{aligned} \lambda_\pm &= \frac{D_{xx}^{-1} v_x^d}{2} \pm \sqrt{\left(\frac{D_{xx}^{-1} v_x^d}{2}\right)^2 + D_{xx}^{-1} \Gamma^P} \\ &= \frac{E}{2} \frac{\tilde{\mu}_x}{D_{xx}} \pm \sqrt{\frac{E^2}{4} \left(\frac{\tilde{\mu}_x}{D_{xx}}\right)^2 + \frac{1}{l_{s0}^2}}, \end{aligned} \quad (97)$$

$$l_{s0} = \sqrt{D_{xx} \tau_{s0}}, \quad (98)$$

which is the same as Eq. 57 from the standard drift-diffusion model.

#### Appendix I: Computational details

Our computational setups are the same as in our prior paper[4] (some data of this paper are openly available). The ground-state electronic structure, phonons, as well as the e-ph matrix elements are firstly calculated using DFT with relatively coarse  $k$  and  $q$  meshes in the open-source DFT plane-wave code JDFTx[34].

For GaAs, WSe<sub>2</sub> and graphene-*h*-BN, the lattice constants are taken 5.653, 3.32 and 2.465 Å respectively, as in our previous work[35, 36]. For GaN, we use relaxed lattice constants with  $a=3.103$  Å and  $c=5.044$  Å. We use PBE exchange-correlation functional[37], except that SCAN functional[38] is used for GaAs as in our previous work[35]. We use Optimized Norm-Conserving Vanderbilt (ONCV) pseudopotentials[39] with spin-orbit coupling. The plane-wave cutoff energies are 34, 64, 74 and 74 Ry for GaAs, WSe<sub>2</sub>, graphene-*h*-BN and GaN respectively. For graphene-*h*-BN, the DFT+D2 correction method[40] with scale factor  $s_6 = 0.5$  is used, to be consistent with our previous work.[36]. The DFT calculations use  $24^3$ ,  $12^2$ ,  $28 \times 28 \times 20$  and  $24^2$   $k$  meshes for GaAs, WSe<sub>2</sub>, GaN and graphene-*h*-BN respectively. The phonon calculations employ  $4^3$ ,  $6^2$ ,  $4^3$  and  $6^2$  supercells respectively through finite difference calculations.

We then transform all quantities from plane wave basis to maximally localized Wannier function basis[41] and interpolate them[42] to substantially finer  $k$  and  $q$  meshes. For WSe<sub>2</sub>, GaAs, GaN and graphene-*h*-BN, the Wannierizations use 22, 16, 24 and 54 Wannier functions, respectively. The inner (or frozen) energy windows include 14, 8, 12 and 16 valence bands, respectively. The upper bounds of inner windows are 2.5 eV, 2.9 eV, 6.6 eV and 14 eV higher than CBM (conduction band minimum), respectively. The outer (disentanglement) energy windows are tens of eV wider than the inner ones. For each material, we do Wannier fittings starting from tens of or hundreds of initial sets of random Wannier centers, and select one set having smallest errors in key quantities for spin decay—band-edge energy splittings, spin-mixing parameters, and spin-orbit fields. The Wannier interpolation approach fully accounts for polar terms in the e-ph matrix elements and phonon dispersion relations, using the approach of Refs. 43 and 44 for the 3D and 2D systems.

For the relaxation and diffusion problems, we only include electronic states close to VBM energy  $E^{\text{vbm}}$ , CBM energy  $E^{\text{cbm}}$  or Fermi level  $E_F$ . More explicitly, we include states within the energy window  $[E^{\text{ref}} - n^w k_B T, E^{\text{ref}} + n^w k_B T]$ , where  $E^{\text{ref}}$  is  $E^{\text{vbm}}$  or  $E^{\text{cbm}}$  for semiconductors and is  $E_F$  for metallic systems.  $n^w$  is typically 7-14, depending on material, temperature, etc. Typically, there are about 2000-7000 states being included for the calculations of  $\tau_s$  and  $l_s$ . For example, for graphene-*h*-BN, the fine  $k$  and  $q$  meshes are  $480 \times 480$  and  $n^w=10$ , leading to  $\approx 2200$  states within the energy window. We have checked the convergence of  $\tau_s$  and  $l_s$  with the number of  $k$ -points and  $n^w$ , and the convergence errors are found within 10%. The energy-conservation smearing parameter  $\sigma_G$  is chosen to be comparable or smaller than  $k_B T$  for each calculation, e.g.,  $\sigma_G$  is typically 0.02 eV for 300 K.  $\tau_s$  and  $l_s$  are computed by our python script using physical quantities at fine meshes.

Overall computational demands are moderate. Most jobs run on one or two Intel Xeon Gold 6248R (48 cores) or 6348 (56 cores) processors. Phonon calculations re-

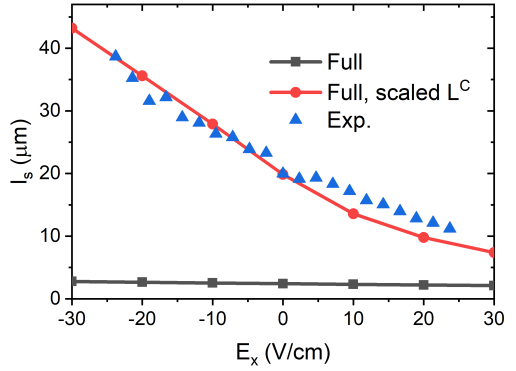


FIG. 6. Calculated  $l_s(E_x)$  of electrons of bulk germanium (Ge) at 300 K by solving full EVP, compared with experimental data from Ref. 16 measured using inverse spin-Hall effect. “scaled  $L^C$ ” means that the scattering term is scaled by a constant to fit the experimental value of  $l_{s0}$ . Note that experimental ranges of room-temperature  $\tau_{s0}$  and  $l_{s0}$  of Ge across different papers are both quite large[45–48] - experimental  $\tau_{s0}$  ranges from 0.25 ns to 132 ns, while experimental  $l_{s0}$  ranges from less than 0.5 μm to 34 μm. Our predicted  $\tau_{s0}$  and  $l_{s0}$  are 0.64 ns and 2.4 μm (without a scaling factor of  $L^C$ ), within the experimental ranges but much shorter than values from Refs. 16 (giving  $l_{s0}$  of 20 μm) and 47 (giving  $\tau_{s0}$  of 132 ns and  $l_{s0}$  of 34 μm).

quire a few to tens of hours. Wannier fitting, depending on the number of initial trial sets, totally takes from a few minutes to tens of hours. A single Wannier interpolation typically completes in tens of minutes to a few hours. Each spin-decay simulation (at a given electric field) by our python script requires between a few minutes and three hours, strongly dependent on the chosen  $k$ -point density and number of bands.

#### Appendix J: About comparison with experiments

In this work, we carry out theoretical studies of the electric-field effects on  $\tau_s$  and  $l_s$  of a few relatively simple materials. The comparisons with experiments are not simple due to several issues:

(i) We consider spin decay only due to only e-ph scattering. However, in realistic samples, impurity scattering can be crucial. In fully *ab initio* simulations, the inclusion of impurity is highly demanding, requiring large supercell calculations and precise knowledge of impurity types and concentrations.

(ii) The experimental materials may be too difficult to be modeled in full *ab initio* simulations. For instance, fully *ab initio* modelings of quantum well, quantum wire and graphene on SiO<sub>2</sub>, studied in some experimental studies[15, 49, 50], require extremely large supercells. Moreover, our studied systems may be quite different from those in experiments, in carrier density, substrate, temperature, etc.

(iii) Both theoretical and experimental data may have

significant uncertainties or errors. Theoretical results are limited by the accuracy of DFT with specific functionals, while experimental values are sensitive to various factors such as sample quality, measurement technique and data analysis method. For instance, the experimental values of room-temperature  $l_{s0}$  of graphene samples, GaN and Pt, RuO<sub>2</sub> range from a few to 31  $\mu\text{m}$ , 135-510 nm, 1-11 nm and 2-12 nm, respectively, in the literature[3, 4, 8].

Given that the primary goals of this work are to establish a fully *ab initio* framework for computing  $\tau_s(E)$  and  $l_s(E)$  and to demonstrate its application to a few representative systems while validating various approximate methods, we would like to avoid the complexities above, which may introduce confusions of the readers. Therefore, we do not present direct comparisons with experimental data in the main text.

Overall, there exist limited number of experimental studies of the effect of periodic-direction electric field on  $\tau_s$  or  $l_s$ . For  $l_s$ , to the best of our knowledge, there exist only three papers (Refs. 49, 15 and 16) directly presenting experimental data of  $l_s$  as a function of periodic-direction electric field. Since the materials in Refs. 49 and 15 are difficult to be simulated, we will try to study a relatively simple material in Ref. 16 - bulk germanium (Ge).

Standard PBE functional incorrectly predicts Ge to be metallic, whereas it is known that Ge is a semiconductor of band gap about 0.66 eV and CBM located at  $L$  point. Therefore, we select the MGGAC functional[51, 52], as it correctly captures the semiconducting nature of Ge, yielding a band gap of 0.94 eV and the CBM at  $L$  point. Furthermore, MGGAC provides lattice constants in agreement with both experimental and PBE values. This ensures the accuracy of force simulation with MG-GAC, which is crucial for phonon and electron-phonon simulations. Hybrid functionals are not used due to their prohibitive computational cost, which makes subsequent phonon and electron-phonon calculations infeasible.

With MGGAC functional, we simulate  $l_s$  of Ge at 300 K. Our obtained  $l_{s0}$  of Ge is 2.4  $\mu\text{m}$ , which is within the experimental range from less than 0.5  $\mu\text{m}$  to 34  $\mu\text{m}$ ,[45-48] but much shorter than 20  $\mu\text{m}$  from Ref. 16 and 34  $\mu\text{m}$  from Ref. 47. We find that if theoretical  $l_{s0}$  is tuned 20  $\mu\text{m}$  to by multiplying a scaling factor to the scattering term  $L^C$ , our theoretical values of  $l_s(E_x)$  are in agreement with experimental data, as illustrated in Fig. 6.

## Appendix K: The derivation of Eq. 62 from 1-RR simulation

Within a minimum 1-RR simulation, for  $\tau_{sx}(E_x)$ , we set  $V^{KR(L)}$  as

$$V^{KR} = \{U_{sx}^{tR}, -L^E U_{sx}^{tR}\}, \quad (99)$$

$$V^{KL} = \{U_{sx}^{tL}, -L^{E,\dagger} U_{sx}^{tL}\}. \quad (100)$$

Here we considered the fact that it is unnecessary to include  $L^{E0} U_{sx}^{tR(L)}$  as  $U_{sx}^{tR(L)}$  is eigenvector of  $L^{E0}$ . With

such  $V^{KR(L)}$ , we have

$$I^K = \begin{bmatrix} 1 & -L_1^{E,xx} \\ -L_1^{E,xx} & L_2^{E,xx} \end{bmatrix}, \quad (101)$$

$$-L^{E0K} = \begin{bmatrix} \Gamma_{s0}, & U_{sx}^{tL,\dagger} L^{E0} L^E U_{sx}^{tR} \\ U_{sx}^{tL,\dagger} L^E L^{E0} U_{sx}^{tR}, & -U_{sx}^{tL,\dagger} L^E L^{E0} L^E U_{sx}^{tR} \end{bmatrix}, \quad (102)$$

$$\approx \begin{bmatrix} \Gamma_{s0}, & -\tau^{-1} L_1^{E,xx} \\ -\Gamma_{s0} L_1^{E,xx}, & -U_{sx}^{tL,\dagger} L^E L^{E0} L^E U_{sx}^{tR} \end{bmatrix} \quad (103)$$

$$-L^{EK} = \begin{bmatrix} -L_1^{E,xx} & L_2^{E,xx} \\ L_2^{E,xx} & -L_3^{E,xx} \end{bmatrix}, \quad (104)$$

$$L_n^{E,xx} = U_{sx}^{tL,\dagger} (L^E)^n U_{sx}^{tR}. \quad (105)$$

Typically, it is found that  $L_1^{E,xx}$  and  $L_3^{E,xx}$  are negligible compared with matrix elements, so that we approximate them as 0. Define

$$\tau^{-1} = \frac{-U_{sx}^{tL,\dagger} L^E L^{E0} L^E U_{sx}^{tR}}{L_2^{E,xx}}, \quad (106)$$

$$\langle \Omega_{E,x}^2 \rangle = -L_2^{E,xx}, \quad (107)$$

where  $\tau$  is an effective lifetime comparable to carrier lifetime. we then have

$$I^K \approx \begin{bmatrix} 1 & 0 \\ 0 & -\langle \Omega_{E,x}^2 \rangle \end{bmatrix}, \quad (108)$$

$$-L^{E0K} \approx \begin{bmatrix} \Gamma_{s0} & 0 \\ 0 & -\tau^{-1} \langle \Omega_{E,x}^2 \rangle \end{bmatrix}$$

$$-L^{EK} \approx \begin{bmatrix} 0 & -\langle \Omega_{E,x}^2 \rangle \\ -\langle \Omega_{E,x}^2 \rangle & 0 \end{bmatrix}. \quad (109)$$

Without external magnetic field, zero-electric-field spin relaxation rate  $\Gamma_{s,x}^0$  should be a real value and  $\Gamma_{s,x}^0 = \tau_{sx}^{-1}(E_x = 0)$ . With the above matrices, by solving the reduced EVP Eq. 34, we obtain electric-field-dependent spin relaxation rates

$$\Gamma_{s\pm}(E_x) = \frac{\tau^{-1} + \tau_{sx}^{-1}(E_x = 0)}{2} \pm \frac{\sqrt{(\tau^{-1} - \tau_{sx}^{-1}(E_x = 0))^2 - 4 \langle \Omega_{E,x}^2 \rangle}}{2}. \quad (110)$$

In our studied  $E$  range,  $(4 \langle \Omega_{E,x}^2 \rangle)^{1/2} \ll \tau^{-1} - \tau_{sx}^{-1}(E_x = 0)$  is satisfied. Therefore, the slower (spin) relaxation rate is approximately

$$\Gamma_{s-}(E_x) \approx \tau_{sx}^{-1}(E_x = 0) + (\tau^{-1} - \tau_{sx}^{-1}(E_x = 0))^{-1} \langle \Omega_{E,x}^2 \rangle. \quad (111)$$

In many systems including those studied here,  $\tau_{sx}^{-1}(E_x = 0) \ll \tau^{-1}$  is satisfied. Therefore,

$$\Gamma_{s-}(E_x) \approx \tau_{sx}^{-1}(E_x = 0) + \tau \langle \Omega_{E,x}^2 \rangle, \quad (112)$$

which is exactly Eq. 62.

Finally, we show that  $\langle \Omega_{E,\alpha}^2 \rangle$  is often negligible when spin precession is absent. In such cases, spin relaxation is dominated by EY mechanism. Again, we suppose spins are highly polarized along  $\alpha$  direction or there are two Kramers degenerate bands with one spin-up and the other spin-down. In these cases, spin matrix (in Bloch basis)  $s_\alpha$  is approximately  $k$ -independent. Therefore, we have

$$U_{sx}^{tR} \approx \rho_k^{s_\alpha} = c^\rho \frac{df_k}{d\epsilon} s_\alpha, \quad (113)$$

$$U_{sx}^{tL} \approx \varrho^{s_\alpha} = c^\varrho s_\alpha, \quad (114)$$

where  $c^\rho$  and  $c^\varrho$  are real constants and their choices must satisfy  $\varrho^{s_\alpha} \rho^{s_\alpha} = 1$ .

We also suppose  $\xi$ -part of  $L^E$  is negligible, which is satisfied in one-band systems and in many systems if smooth basis functions are chosen. Thus, we can approximate  $L^E \approx \frac{eE_x}{\hbar} \frac{d}{dk_x}$ . From integration by parts, we can easily prove that  $\langle \Omega_{E,x}^2 \rangle = -L_2^{E,xx} \approx 0$ .

## Appendix L: Obtaining Eq. 63 from approximate 0-RR simulation

Below we will show that in a given two-band system, spin relaxation in the case of a non-zero  $E_x$  and  $\mathbf{B}=0$  is similar to spin relaxation in another case of  $E_x=0$  and  $\mathbf{B}$  equal to  $\mathbf{B}^{E_x}$  defined in Eq. 63.

Consider a two-band system, whose bands are originally Kramers degenerate and splitted by spin-orbit fields  $\mathbf{B}_k^{\text{soc}}$  and external magnetic field  $\mathbf{B}$ , the system Hamiltonian reads

$$H_k = \epsilon_k + H_k^{\text{soc}} + H^{\text{sz}}, \quad (115)$$

$$H_k^{\text{soc}} = \frac{\mu_B g_0 \hbar}{2} \mathbf{B}_k^{\text{soc}} \cdot \sigma, \quad (116)$$

$$H^{\text{sz}} = \frac{\mu_B g_0 \hbar}{2} \mathbf{B} \cdot \sigma. \quad (117)$$

In this case, we have (with original eigenbasis where bands are Kramers degenerate)

$$\rho_k^{s_\alpha} = c^\rho \frac{df_k}{d\epsilon} \sigma_\alpha, \quad (118)$$

$$\varrho_k^{s_\alpha} = c^\varrho \sigma_\alpha, \quad (119)$$

with  $c^\rho$  and  $c^\varrho$  real constants and  $\langle \varrho^s | \rho^s \rangle = 1$ . Therefore, we have (defining  $L^{e0} = L^e(\mathbf{B} = 0)$ )

$$L^{e0} \rho^{s_\alpha} \approx \frac{-i}{\hbar} [H_k^{\text{soc}}, \rho_k^{s_\alpha}], \quad (120)$$

$$L^{e0} \varrho^{s_\alpha} \approx \frac{-i}{\hbar} [H_k^{\text{soc}}, \varrho_k^{s_\alpha}] \quad (121)$$

Within the 0-RR simulation,  $V^{KR(L)}$  is set as

$$V^{KR(L)} = \{U_{sx}^{tR(L)}, U_{sy}^{tR(L)}, U_{sz}^{tR(L)}\}, \quad (122)$$

with  $U_{s\alpha}^{tR(L)}$  zero-field eigenvector corresponding to the eigenvalue  $\tau_{s0\alpha}^{-1}$ .  $\tau_{s0\alpha}$  is zero-field spin lifetime.

If the scattering is relatively strong, which is usually true, we have  $\tau L^e \rho^{s_\alpha} \ll \rho^{s_\alpha}$  and  $\tau L^e \varrho^{s_\alpha} \ll \varrho^{s_\alpha}$ . According to our prior paper (Ref. 4), we approximately have

$$U_{s\alpha}^{tR} \approx (1 + \tau L^e \rho^{s_\alpha}) \rho^{s_\alpha}, \quad (123)$$

$$U_{s\alpha}^{tL} \approx (1 - \tau L^e \rho^{s_\alpha}) \varrho^{s_\alpha}. \quad (124)$$

With the above  $V^{KR(L)}$ , the reduced EVP at  $E_x=0$  is

$$-L^{E0K} Y^R = Y^R \Gamma_s^{E0}, \quad (125)$$

where

$$-L^{E0K} = \begin{bmatrix} \tau_{s0x}^{-1} - L^{B,xx}, & -L^{B,xy}, & -L^{B,xz} \\ -L^{B,yx}, & \tau_{s0y}^{-1} - L^{B,yy}, & -L^{B,yz} \\ -L^{B,zx}, & -L^{B,zy}, & \tau_{s0z}^{-1} - L^{B,zz} \end{bmatrix}, \quad (126)$$

$$L^{B,\alpha\beta} = U_{s\alpha}^{tL,\dagger} \frac{-i}{\hbar} [H^{\text{sz}}, U_{s\beta}^{tR}]. \quad (127)$$

Since  $\tau L^e \rho^{s_\alpha} \ll \rho^{s_\alpha}$  and  $\tau L^e \varrho^{s_\alpha} \ll \varrho^{s_\alpha}$ , we have

$$\begin{aligned} L^{B,\alpha\beta} &\approx \text{Tr} \int dk \varrho_k^{s_\alpha} \frac{-i}{\hbar} [H^{\text{sz}}, \rho_k^{s_\beta}] \\ &= \text{Tr} \int dk \varrho_k^{s_\alpha} \frac{-i}{\hbar} \left[ \frac{\mu_B g_0 \hbar}{2} \mathbf{B} \cdot \sigma, \rho_k^{s_\beta} \right] \\ &= \varepsilon_{\gamma\beta\alpha} \mu_B g_0 B_\gamma^{\text{ext}}. \end{aligned} \quad (128)$$

The derivation uses the relation  $[\sigma_\gamma, \sigma_\beta] = 2i\varepsilon_{\gamma\beta\alpha} \sigma_\alpha$ .

Now, we consider the system at  $E_x \neq 0$  but  $\mathbf{B}=0$ . The reduced EVP in this case is

$$-L^{B0K} Y^R = Y^R \Gamma_s^{B0}, \quad (129)$$

where

$$-L^{B0K} = \begin{bmatrix} \tau_{s0x}^{-1} - L_1^{E,xx}, & -L_1^{E,xy}, & -L_1^{E,xz} \\ -L_1^{E,yx}, & \tau_{s0y}^{-1} - L_1^{E,yy}, & -L_1^{E,yz} \\ -L_1^{E,zx}, & -L_1^{E,zy}, & \tau_{s0z}^{-1} - L_1^{E,zz} \end{bmatrix}, \quad (130)$$

$$L_1^{E,\alpha\beta} = U_{s\alpha}^{tL,\dagger} L^E U_{s\beta}^{tR}. \quad (131)$$

$L_1^{E,\alpha\beta}$  can be expressed as the sum of the following four terms (note that  $L^{e,\dagger} = -L^e$ )

$$\begin{aligned} L_1^{E,\alpha\beta} &= \langle \varrho^{s_\alpha} | L^E | \rho^{s_\beta} \rangle + \\ &\quad \langle \varrho^{s_\alpha} | L^E | \tau L^e \rho^{s_\beta} \rangle + \\ &\quad \langle -\tau L^e \varrho^{s_\alpha} | L^E | \rho^{s_\beta} \rangle + \\ &\quad \langle -\tau L^e \varrho^{s_\alpha} | L^E | \tau L^e \rho^{s_\beta} \rangle. \end{aligned} \quad (132)$$

Since  $\tau L^e \rho^{s_\alpha} \ll \rho^{s_\alpha}$  and  $\tau L^e \varrho^{s_\alpha} \ll \varrho^{s_\alpha}$ , the 4th term is negligible.

Integration by parts, the 3rd term of  $L_1^{E,\alpha\beta}$  reads

$$\begin{aligned}
& \langle -\tau L^e \varrho^{s_\alpha} | L^E | \rho^{s_\beta} \rangle \\
& \approx -\frac{e}{\hbar} E_x \text{Tr} \int dk \rho_k^{s_\beta} \frac{d}{dk_x} (-\tau L_k^e \varrho_k^{s_\alpha}) \\
& = \tau \frac{-i}{\hbar} \frac{e}{\hbar} E_x \text{Tr} \int dk \rho_k^{s_\beta} \left[ \frac{dH_k^{\text{soc}}}{dk_k}, \varrho_k^{s_\alpha} \right] \\
& = \tau \frac{-i}{\hbar} \frac{e}{\hbar} E_x \frac{\mu_B g_0 \hbar}{2} \text{Tr} \int dk \rho_k^{s_\beta} \left[ \frac{d\mathbf{B}_k^{\text{soc}}}{dk_x} \cdot \boldsymbol{\sigma}, \varrho_k^{s_\alpha} \right] \\
& = -\varepsilon_{\gamma\beta\alpha} \frac{e\mu_B g_0}{\hbar} E_x \tau \langle \varrho^{s_\beta} | \frac{dB_{k\gamma}^{\text{soc}}}{dk_x} | \rho^{s_\alpha} \rangle. \quad (133)
\end{aligned}$$

The derivation considers  $\varepsilon_{\gamma\alpha\beta} = -\varepsilon_{\gamma\beta\alpha}$ .  $\langle \varrho^{s_\beta} | dB_{k\gamma}^{\text{soc}}/dk_x | \rho^{s_\alpha} \rangle$  can be understood as Fermi-surface average of  $dB_{k\gamma}^{\text{soc}}/dk_x - \langle dB_{k\gamma}^{\text{soc}}/dk_x \rangle$ . Therefore,

$$\begin{aligned}
L_1^{E,\alpha\beta} & \approx \langle -\tau L^e \varrho^{s_\alpha} | L^E | \rho^{s_\beta} \rangle \\
& \approx -\varepsilon_{\gamma\beta\alpha} \frac{e\mu_B g_0}{\hbar} E_x \tau \left\langle \frac{dB_{k\gamma}^{\text{soc}}}{dk_x} \right\rangle, \quad (134)
\end{aligned}$$

Suppose  $\xi$ -part of  $L^E$  is negligible, which is satisfied in many systems if smooth basis functions are chosen. Thus, we can approximate  $L^E \approx \frac{eE_x}{\hbar} \frac{d}{dk_x}$ . From integration by parts, the 1st and 2nd terms of  $L_1^{E,\alpha\beta} - \langle \varrho^{s_\alpha} | L^E | \rho^{s_\beta} \rangle$  and  $\langle \varrho^{s_\alpha} | L^E | \tau L^e \rho^{s_\beta} \rangle$  are both zero. Moreover, from in-

which is the same as  $L^{B,\alpha\beta}$  if  $B_\gamma^{\text{ext}} = -e\hbar^{-1} E_x \tau \langle dB_{k\gamma}^{\text{soc}}/dk_x \rangle$ . This indicates that an electric field  $E_x$  indeed generates an effective magnetic field as defined in Eq. 63.

---

[1] I. Žutić, J. Fabian, and S. D. Sarma, Spintronics: Fundamentals and Applications, *Rev. Mod. Phys.* **76**, 323 (2004).

[2] M. Wu, J. Jiang, and M. Weng, Spin dynamics in semiconductors, *Phys. Rep.* **493**, 61 (2010).

[3] A. Avsar, H. Ochoa, F. Guinea, B. Özyilmaz, B. J. van Wees, and I. J. Vera-Marun, Colloquium: Spintronics in Graphene and Other Two-Dimensional Materials, *Rev. Mod. Phys.* **92**, 021003 (2020).

[4] J. Xu, Predicting and understanding diffusion lengths and lifetimes in solids via a many-body ab initio method: The role of coupled dynamics, *Phys. Rev. Lett.* **135**, 046705 (2025).

[5] J. Li, M. Goryca, K. Yumigeta, H. Li, S. Tongay, and S. A. Crooker, Valley relaxation of resident electrons and holes in a monolayer semiconductor: Dependence on carrier density and the role of substrate-induced disorder, *Phys. Rev. Mater.* **5**, 044001 (2021).

[6] R. Dzhioev, K. Kavokin, V. Korenev, M. Lazarev, N. Poletaev, B. Zakharchenya, E. Stinaff, D. Gammon, A. Bracker, and M. Ware, Suppression of Dyakonov-Perel spin relaxation in high-mobility n-GaAs, *Phys. Rev. Lett.* **93**, 216402 (2004).

[7] H. Li, M. Zhu, Z. Guo, G. Li, J. Shang, Y. Yang, Y. Feng, Y. Lu, Q. Zhang, S. Wang, *et al.*, Spintronics in GaN-Based Semiconductors: Research Progress, Challenges and Perspectives, *Adv. Mater. Technol.* **10**, 2401017 (2025).

[8] R. J. Wesselink, K. Gupta, Z. Yuan, and P. J. Kelly, Calculating spin transport properties from first principles: Spin currents, *Phys. Rev. B* **99**, 144409 (2019).

[9] A. Bose, N. J. Schreiber, R. Jain, D.-F. Shao, H. P. Nair, J. Sun, X. S. Zhang, D. A. Muller, E. Y. Tsymbal, D. G. Schlom, *et al.*, Tilted spin current generated by the collinear antiferromagnet ruthenium dioxide, *Nat. Electron.* **5**, 267 (2022).

[10] J. Xu, H. Takenaka, A. Habib, R. Sundararaman, and Y. Ping, Giant Spin Lifetime Anisotropy and Spin-Valley Locking in Silicene and Germanene from First-Principles Density-Matrix Dynamics, *Nano Lett.* **21**, 9594 (2021).

[11] J. Xu and Y. Ping, Substrate effects on spin relaxation in two-dimensional dirac materials with strong spin-orbit coupling, *npj Comput. Mater.* **9**, 47 (2023).

[12] Z. Yu and M. Flatté, Electric-field dependent spin diffusion and spin injection into semiconductors, *Phys. Rev. B* **66**, 201202 (2002).

[13] Z. Yu and M. Flatté, Spin diffusion and injection in semiconductor structures: Electric field effects, *Phys. Rev. B* **66**, 235302 (2002).

[14] M. Hruška, Š. Kos, S. Crooker, A. Saxena, and D. L. Smith, Effects of strain, electric, and magnetic fields on lateral electron-spin transport in semiconductor epilayers, *Phys. Rev. B* **73**, 075306 (2006).

[15] C. Józsa, M. Popinciuc, N. Tombros, H. Jonkman, and B. Van Wees, Electronic spin drift in graphene field-effect transistors, *Phys. Rev. Lett.* **100**, 236603 (2008).

[16] C. Zucchetti, A. Marchionni, M. Bollani, F. Ciccarelli, M. Finazzi, and F. Bottegoni, Electric field modulation of spin transport, *APL Mater.* **10** (2022).

[17] M. I. Miah, Drift-diffusion crossover and the intrinsic spin

diffusion lengths in semiconductors, *J. Appl. Phys.* **103** (2008).

[18] J. H. Jiang and M. W. Wu, Electron-Spin Relaxation in Bulk III-V Semiconductors from a Fully Microscopic Kinetic Spin Bloch Equation Approach, *Phys. Rev. B* **79**, 125206 (2009).

[19] A. Sekine, D. Culcer, and A. H. MacDonald, Quantum kinetic theory of the chiral anomaly, *Phys. Rev. B* **96**, 235134 (2017).

[20] J. Xu and H. Xiao, Ab initio wannier-representation-based calculations of photocurrent in semiconductors and metals, *Phys. Rev. B* **110**, 064315 (2024).

[21] G. Ventura, D. Passos, J. L. Dos Santos, J. V. P. Lopes, and N. Peres, Gauge covariances and nonlinear optical responses, *Phys. Rev. B* **96**, 035431 (2017).

[22] R. Rosati, R. C. Iotti, F. Dolcini, and F. Rossi, Derivation of Nonlinear Single-Particle Equations via Many-Body Lindblad Superoperators: A Density-Matrix Approach, *Phys. Rev. B* **90**, 125140 (2014).

[23] J. Xu and Y. Ping, Ab Initio Predictions of Spin Relaxation, Dephasing, and Diffusion in Solids, *J. Chem. Theory Comput.* **20**, 492 (2023).

[24] R. C. Iotti, E. Ciancio, and F. Rossi, Quantum transport theory for semiconductor nanostructures: A density-matrix formulation, *Phys. Rev. B* **72**, 125347 (2005).

[25] R. Silva, F. Martín, and M. Ivanov, High harmonic generation in crystals using maximally localized wannier functions, *Phys. Rev. B* **100**, 195201 (2019).

[26] N. Marzari, A. A. Mostofi, J. R. Yates, I. Souza, and D. Vanderbilt, Maximally localized wannier functions: Theory and applications, *Rev. Mod. Phys.* **84**, 1419 (2012).

[27] J. Xu, A. Habib, S. Kumar, F. Wu, R. Sundararaman, and Y. Ping, Spin-Phonon Relaxation from a Universal Ab Initio Density-Matrix Approach, *Nat. Commun.* **11**, 2780 (2020).

[28] J. MacDonald, Successive approximations by the Rayleigh-Ritz variation method, *Phys. Rev.* **43**, 830 (1933).

[29] J. Liesen and Z. Strakos, *Krylov subspace methods: principles and analysis* (Numerical Mathematics and Scie, 2013).

[30] S. Poncé, W. Li, S. Reichardt, and F. Giustino, First-principles calculations of charge carrier mobility and conductivity in bulk semiconductors and two-dimensional materials, *Rep. Prog. Phys.* **83**, 036501 (2020).

[31] R. C. Iotti and F. Rossi, Phonon-induced dissipation and decoherence in solid-state quantum devices: Markovian versus non-Markovian treatments, *Eur. Phys. J. B* **90**, 1 (2017).

[32] J. Xu, K. Li, U. N. Huynh, M. Fadel, J. Huang, R. Sundararaman, V. Vardeny, and Y. Ping, How spin relaxes and dephases in bulk halide perovskites, *Nat. Commun.* **15**, 188 (2024).

[33] J. Xu, Spin relaxation in graphite due to spin-orbit-phonon interaction from a first-principles density matrix approach, *Phys. Rev. B* **110**, 144307 (2024).

[34] R. Sundararaman, K. Letchworth-Weaver, K. A. Schwarz, D. Gunceler, Y. Ozhabes, and T. A. Arias, JDFTx: Software for Joint Density-Functional Theory, *SoftwareX* **6**, 278 (2017).

[35] J. Xu, A. Habib, R. Sundararaman, and Y. Ping, Ab initio ultrafast spin dynamics in solids, *Phys. Rev. B* **104**, 184418 (2021).

[36] A. Habib, J. Xu, Y. Ping, and R. Sundararaman, Electric fields and substrates dramatically accelerate spin relaxation in graphene, *Phys. Rev. B* **105**, 115122 (2022).

[37] J. P. Perdew, K. Burke, and M. Ernzerhof, Generalized Gradient Approximation Made Simple, *Phys. Rev. Lett.* **77**, 3865 (1996).

[38] J. Sun, A. Ruzsinszky, and J. P. Perdew, Strongly Constrained and Appropriately Normed Semilocal Density Functional, *Phys. Rev. Lett.* **115**, 036402 (2015).

[39] D. R. Hamann, Optimized Norm-Conserving Vanderbilt Pseudopotentials, *Phys. Rev. B* **88**, 085117 (2013).

[40] S. Grimme, Semiempirical GGA-Type Density Functional Constructed with a Long-Range Dispersion Correction, *J. Comput. Chem.* **27**, 1787 (2006).

[41] N. Marzari and D. Vanderbilt, Maximally Localized Generalized Wannier Functions for Composite Energy Bands, *Phys. Rev. B* **56**, 12847 (1997).

[42] F. Giustino, Electron-Phonon Interactions from First Principles, *Rev. Mod. Phys.* **89**, 015003 (2017).

[43] C. Verdi and F. Giustino, Fröhlich Electron-Phonon Vertex from First Principles, *Phys. Rev. Lett.* **115**, 176401 (2015).

[44] T. Sohier, M. Gibertini, M. Calandra, F. Mauri, and N. Marzari, Breakdown of optical phonons' splitting in two-dimensional materials, *Nano Lett.* **17**, 3758 (2017).

[45] K. Hamaya, Y. Fujita, M. Yamada, M. Kawano, S. Yamada, and K. Sawano, Spin transport and relaxation in germanium, *J. Phys. D: Appl. Phys.* **51**, 393001 (2018).

[46] C. Rinaldi, S. Bertoli, M. Asa, L. Baldrati, C. Manzoni, M. Marangoni, G. Cerullo, M. Bianchi, R. Sordan, R. Bertacco, *et al.*, Determination of the spin diffusion length in germanium by spin optical orientation and electrical spin injection, *J. Phys. D: Appl. Phys.* **49**, 425104 (2016).

[47] C. Zucchetti, M. Bollani, G. Isella, M. Zani, M. Finazzi, and F. Bottegoni, Doping dependence of the electron spin diffusion length in germanium, *APL Mater.* **7** (2019).

[48] M. Yamada, T. Ueno, T. Naito, K. Sawano, and K. Hamaya, Experimental extraction of donor-driven spin relaxation in n-type nondegenerate germanium, *Phys. Rev. B* **104**, 115301 (2021).

[49] J. H. Kwon, H. C. Koo, J. Eom, J. Chang, and S.-H. Han, Electric field effect on spin diffusion in a semiconductor channel, *IEEE Trans. Magn.* **44**, 2647 (2008).

[50] S. Pramanik, S. Bandyopadhyay, and M. Cahay, Spin dephasing in quantum wires, *Phys. Rev. B* **68**, 075313 (2003).

[51] B. Patra, S. Jana, L. Constantin, and P. Samal, Relevance of the pauli kinetic energy density for semilocal functionals, *Phys. Rev. B* **100** (2019).

[52] A. Patra, S. Jana, P. Samal, F. Tran, L. Kalantari, J. Doumont, and P. Blaha, Efficient band structure calculation of two-dimensional materials from semilocal density functionals, *J. Phys. Chem. C* **125**, 11206 (2021).